General Disclaimer

One or more of the Following Statements may affect this Document

- This document has been reproduced from the best copy furnished by the organizational source. It is being released in the interest of making available as much information as possible.

- This document may contain data, which exceeds the sheet parameters. It was furnished in this condition by the organizational source and is the best copy available.

- This document may contain tone-on-tone or color graphs, charts and/or pictures, which have been reproduced in black and white.

- This document is paginated as submitted by the original source.

- Portions of this document are not fully legible due to the historical nature of some of the material. However, it is the best reproduction available from the original submission.

Produced by the NASA Center for Aerospace Information (CASI)

FIRST QUARTERLY REPORT

ON THE CONSTRUCTION AND

TEST OF A

DUAL PATCH MULTI-ELEMENT
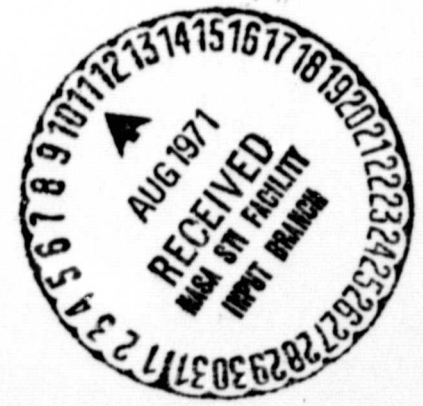
RADIANT COOLER

R. V. Annable and J. F. Lodder

ITT Aerospace/Optical Division
Electro-Optical Operations
Fort Wayne, Indiana 46803

January 1971

Interim Report for Period 17 September to 17 December 1970

Prepared for

GODDARD SPACE FLIGHT CENTER
Greenbelt, Maryland 20771

1. Report No.	2. Government Accession No.	3. Recipient's Catalog No.
4. Title and Subtitle FIRST QUARTERLY REPORT ON THE CONSTRUCTION AND TEST OF A DUAL PATCH MULTI-ELEMENT RADIANT COOLER		5. Report Date January 1971
		6. Performing Organization Code
7. Author(s)		8. Performing Organization Report No.
9. Performing Organization Name and Address ITT Aerospace/Optical Division Electro-Optical Operations Fort Wayne, Indiana 46803		10. Work Unit No.
		11. Contract or Grant No. NAS5-21132
12. Sponsoring Agency Name and Address Goddard Space Flight Center Greenbelt, Maryland 20771 I. L. Goldberg, Code 731		13. Type of Report and Period Covered Interim 17 Sept. - 17 Dec. 1970
		14. Sponsoring Agency Code
15. Supplementary Notes		

16. Abstract

This report covers the start of the second phase of the program, the construction and test of a dual patch multi-element radiant cooler. Studies showed that directional reflectivity effects at the inner cone surface are not critical to cooler performance, but that non-specular effects are. Preliminary measurements showed that one can achieve an effective cone wall emissivity below the design value of 0.05. Cold traps and baffles replaced the anti-frost enclosures in the initial design. Detailed mechanical design was completed, including the preparation of drawings.

17. Key Words	18. Distribution Statement		
19. Security Classif. (of this report)	20. Security Classif. (of this page)	21. No. of Pages	22. Price

PREFACE

This report covers the first quarter of the contract's second phase, the construction and test of a dual patch multi-element radiant cooler. A study of the inner cone surface properties showed that: (a) directional reflectivity produces only a relatively small increase in effective emissivity and (b) reduction of non-specular reflectivity to an acceptably low value requires optical finishing of the cone walls. The anti-frost design of the radiant cooler was considered in detail; the anti-frost enclosures were replaced by cold traps and baffles. Experimental studies were started on the thermal properties of multilayer insulation and inner cone surfaces as they apply to radiant coolers. Preliminary results indicated an upper limit to effective cone wall emissivity of 0.048, which is below the nominal design value (see design study report of July 1970). Heaters were designed for initial outgassing and for simulation of cooler thermal loads. The detailed mechanical design of the dual patch cooler was completed; the assembly drawings are included in the report.

TABLE OF CONTENTS

Page

LIST OF ILLUSTRATIONS

LIST OF TABLES

1.0   INTRODUCTION

The construction and test phase of the program was begun on 17 September 1970, following the approval of the design study report (Design of a Dual Patch Multi-Element· Radiant Cooler, July 1970). The properties of the inner cone surface were investigated both theoretically (Section 2.0) and experimentally (Section 4.2). The theoretical study showed that non-specular reflectivity influences thermal performance more than directional reflectivity (i.e., variation with incidence angle). The study also revealed the need for an optical finish on the inner cone surface   (Section 2.2 and Appendix). The experimental measurements indicated that we can achieve an effective specular cone wall emissivity less than the design value of 0.05.

The anti-frost enclosures described in Section 6.3 of the design study report were replaced by cold traps and baffles (Section 3.0). Paths were provided for outgassing the insulation blanket below the patches. The ports needed for optical coupling to the cooler were designed and sealed with windows to separate the cooler into two compartments. This was done to prevent the interchange of outgassing products and contaminants. The heaters needed for initial cooler outgassing were designed (Section 5.0) together with those required during cooler operation. In addition, an experimental study was begun on the properties of multilayer insulation (Section 4.1).

The detailed mechanical design (IIIA in the design study report) of the radiant cooler was completed. A set of assembly and parts drawings was prepared and the construction of parts nearly completed.

2.0 CONE SURFACE PROPERTIES

Obtaining a low radiative coupling between the cone walls and patch has been a continuing problem in radiant coolers. Based on specular reflection at the walls, the apparent or effective cone surface emissivity has consistently exceeded the hemispherical emissivity. Analysis of the HRIR single-stage cooler[1] (see list of references in Section 2.3) showed that the apparent surface emissivity of the cone walls was in the range from 0.062 to 0.086, considerably above the hemispherical emissivity of a gold-coated surface (0.02 to 0.05). The cone wall surfaces of the two-stage radiant cooler showed an effective emissivity of 0.07 when the hemispherical emissivity was 0.05[2]. This seemed to be largely the result of waves and wrinkles in the aluminized mylar used as a cone wall reflector.

The design and analysis of radiant coolers after completion of the work described in Reference 2 has therefore been based on an apparent specular emissivity of 0.05 to 0.07. We felt that a maximum value equal to that of wavy aluminized mylar surface should be easy to achieve. Alas, such was not the case. The most recent and best documented example is the single-stage cooler designed for the ITOS radiometer. A careful and accurate analysis was made using the specular reflection model and an apparent cone wall emissivity of 0.07. Experimental results, however, indicated an apparent emissivity about twice this value [3]. On top of that, the measured hemispherical emissivity of a reflector prepared according to the procedure used in this cooler had the satisfyingly low value of 0.017 ± 0.0015[4].

The large relative increase in the apparent cone surface emissivity may be the result of:

a. The increase in emissivity of a metallic reflector with an increase in emission angle relative to the surface normal.

b. A diffuse, or in general non-specular, component of reflection.

c. Surface cavities which introduce additional cone wall reflections.

A study of the first effect has shown that it produces only relatively small increases in the apparent emissivity (Section 2.1). Samples of epoxy-coated aluminum with significant surface cavities have been produced[4]. The surface looked irregular to the eye. Its emissivity was about four times that of a sample spray-coated with polyurethane varnish (ITOS procedure) and a strong function of the emission angles covered. For example, the emissivity over an entire hemisphere was 0.07, but it decreased to 0.032 when the emission was restricted to angles less than 72° from the surface normal. On the other hand, when the surface irregularities have small slopes, the cavity effect is small or entirely absent. In particular, such cavities were not present in the spray-coated surfaces.

The cause for the large increase in the specular emissivity of cone wall surfaces as seen from the patch in a radiant cooler therefore seems to be a non-specular component of reflection at the surfaces. In the limiting (worst) case of a small fraction δ of the reflection is diffuse and the hemispherical emiss... is ϵ, the apparent specular emissivity is $\epsilon + \delta$ [5]. Thus for $\epsilon = 0.02$ and $\delta = 0.02$ (2% diffuse reflection), the apparent emissivity is 0.04 or twice the hemispherical value. The limiting case occurs for concentric or coaxial geometries. The radiative exchange is then a minimum for specular reflection at the outer surface and a maximum for diffuse reflection [6].

The nature of the reflection at a surface is a very sensitive function of its roughness (Section 2.2). For example, a root-mean-square roughness (the rms devia-tion of the surface from a plane representing the mean height) of only 0.008 of the wave-length of the incident radiation produces a fractional non-specular reflection component of 0.01 or 1%. The use of optically polished cone surfaces is therefore indicated even for use at the wavelengths associated with cone wall emission.

The theory and experiments of Bennett and Porteus (Section 2.2), provide an explanation of past results with cone wall surfaces. A metallic film evaporated onto a rough surface will, for the most part, replicate the roughness of the surface. The roughness of a rolled, cold drawn, or machined surface [7] will produce a large com-ponent of non-specular reflection at the wavelengths of interest. Coating the surface with an epoxy or plastic will reduce the roughness and therefore the non-specular component. At the same time, the apparent specular emissivity as seen from the patch will decrease. However, the epoxy or plastic surface is still rough compared to an optically polished surface. Also, an additional non-specular reflection component is introduced by scattering off bubbles, dust, and other included matter. Finally, the irregularities of the slope must be kept small to prevent the introduction of surface cavities. All these factors indicate that the entire epoxy coating process would tend to be non-reproducible.

The details of surface roughness as studied by Bennett and Porteus are described in Section 2.2 and are used to make an estimate of the optical finish required for the cone walls of a radiant cooler. A specification on the cone walls for the multi-element radiant cooler is given in the Appendix.

2.1 Directional Emissivity of a Metallic Reflector

The emissivity of an optically smooth metallic reflector as a function of angle θ from the surface normal may be derived from Fresnel's equations for the reflection of electromagnetic waves. The results for unpolarized radiation are [8]

$$\epsilon (\theta) = 1/2 \cdot \epsilon_\perp (\theta) \left[\frac{a^2 + b^2 + \sin^2 \theta}{\cos^2 \theta \cdot (a^2 + b^2 + 2a \sin \theta \tan \theta + \sin^2 \tan^2 \theta)} \right]$$

where $\epsilon_\perp(\theta)$ = $\dfrac{4a \cos \theta}{a^2 + b^2 + 2a \cos \theta + \cos^2 \theta}$

$a^2 + b^2$ = $[(n^2 - k^2 - \sin^2 \theta)^2 + 4n^2 k^2]^{1/2}$

$2a$ = $\sqrt{2} \times [a^2 + b^2 + n^2 - k^2 - \sin^2 \theta]^{1/2}$

n = refractive index

k = extinction coefficient

If $\epsilon(\theta)$ is represented as function of $\sin^2 \theta$ using linear coordinates, the area under the resultant curve is equal to the hemispherical emissivity[9]. And, in general, the emissivity over a partial hemisphere from $\sin^2 \theta = c$ to $\sin^2 \theta = 1$ is given by

$$\epsilon(\Delta \theta) = \frac{1}{1-c} \int_c^1 \epsilon(x) \cdot dx,$$

where x = $\sin^2 \theta$.

The values of n and k for good conductors in the infrared wavelength region may be calculated from the Drude-Zener theory[10]. Bennett, Silver, and Ashley[11] show that agreement between their theory and experimental measurements in the case of evaporated aluminum requires that the film be prepared under ultra-high vacuum conditions (10^{-8} to 10^{-9} Torr). The mathematical expressions used by Bennett, et. al., are

$$n^2 - k^2 = 1 - \frac{\omega_p^2}{\omega^2 + \frac{1}{\gamma^2}}$$

$$nk = \frac{1}{2 \omega \gamma} \left[\frac{\omega_p^2}{\omega^2 + \frac{1}{\gamma^2}} \right]$$

where ω is the angular frequency and γ the relaxation time. The plasma frequency ω_p is given by

$$\omega_p = \left(\frac{4 \pi N_{eff} e^2}{m} \right)^{1/2}$$

where for a metal N_{eff} is the "effective" free-electron density, e the electronic charge, and m the free electron mass.

The relaxation time is the interval between collisions of an electron with the lattice and is given by

$$\gamma = \frac{m \sigma_0}{N_{eff} e^2}$$

where σ_0 is the bulk d-c conductivity.

The normal reflectivity for metals in the infrared is given by[11]

$$R = 1 - (2\omega/\pi \sigma_0)^{1/2} \cdot [(1 + \omega^2 \gamma^2)^{1/2} - \omega\gamma]^{1/2}$$

where σ_0 is in electrostatic units. At very long wavelengths ($\omega\gamma \ll 1$), this becomes the Hagen-Rubens relation

$$R = 1 - (2\omega/\pi\sigma_0)^{1/2}$$

This equation predicts that the emissivity is inversely proportional to the square root of the wavelength, in sharp disagreement with experimental data on metals in the infrared. In fact, the original measurements by Hagen and Rubens showed agreement only at $25.5\,\mu$m for heated samples[12].

Experimental measurements[11, 13] show that the emissivity of metallic reflectors varies only slowly with wavelength in the infrared region, a fact noted by Scott[14]. Unfortunately, some theoretical studies of the radiative transfer between low-emissivity specular surfaces at and below room temperature have been based on the Hagen-Rubens relation (e.g., [15]).

For aluminum, the d-c bulk conductivity is 3.178×10^{17} esu and the number of effective free electronic/atom, 2.6. The number of atoms in a cubic centimeter of Al (at 20°C) is

$$6.025 \times 10^{23} \; \frac{\text{atoms}}{\text{gm-moles}} \; \times \; \frac{2.70}{26.98} \; \frac{\text{gm-moles}}{\text{cm}^3} = 6.029 \times 10^{22}.$$

so that

$$N_{eff} = 1.568 \times 10^{23} \; \text{electrons/cm}^3$$

The corresponding relaxation time is

$$\gamma = 8.002 \times 10^{-15} \; \text{sec}$$

for $m = 9.108 \times 10^{-28}$ gms and $e = 4.803 \times 10^{-10}$ esu, and the plasma frequency

$$\omega_p = 2.230 \times 10^{16} \; \text{radians/sec.}$$

As previously noted, the infrared emissivity of a metallic film is a weak function of wavelength. We may therefore select a representative wavelength, say $20\,\mu$m, for the emission from a surface in the temperature range typical of cone walls in a radiant cooler. For aluminum at $20\,\mu$m, we obtain

$$n = 81.9$$

$$k = 164$$

The penetration of the reflected electromagnetic wave into the metallic film is measured by its optical skin depth

$$\delta = \frac{\lambda}{2 \pi k}$$

or the distance in which the amplitude of the electric vector drops to 1/e of its initial value (and the intensity of the reflected wave to $1/e^2$). For $\lambda = 20 \mu m$ and $k = 164$, δ is $0.0194 \mu m$ or 7.64×10^{-7} inch.

The directional emissivity $\epsilon (\theta)$ of UHF aluminum was determined for angles (θ) from $0°$ to $90°$ using the calculated values of n and k at a wavelength of $20 \mu m$ (81.9 and 164, respectively). The results are listed in Table 2-1 in terms of $x = \sin^2 \theta$.

The partial hemispherical emissivity $\epsilon (\Delta \theta)$ over the range from $x = c$ to $x = 1$ was calculated using a summation approximation to the integral. The results are given in Table 2-2 for the range from $c = 0$ to $c = 0.50$ or $\theta = 0°$ to $\theta = 45°$. The value for $c = 0$ is the emissivity over an entire hemisphere or simply the hemispherical emissivity. It has a value 1.33 times that of the normal emissivity ($\epsilon (\theta)$ at $\theta = 0°$), the theoretical limiting ratio for a high conductivity metal [16]. The partial hemispherical emissivity over the angular range from $45°$ to $90°$ is 23.6% larger than the hemispherical emissivity.

2.2 Relation Between Surface Roughness and Specular Reflectance

Davies[17] developed an expression relating specular reflectance and rms roughness by means of a statistical treatment of reflection of electro-magnetic waves from a rough surface. The theory was extended to the optical region (visible and infrared) by Bennett and Porteus[18-20]. The subject is also covered in a book by Beckman and Spizzichino[21]. When multiple reflections (cavity effects) are negligible, the principal effect of surface roughness is to convert part of the specular reflectance into non-specular while maintaining the total reflectance equal to that of a perfectly smooth surface of the same material.

For a root mean square deviation σ of the surface from its mean surface limit and a wavelength λ, the specular reflectance at normal incidence is given by

$$R_s = R_0 \exp [- (4 \pi \sigma /\lambda)^2]$$

where R_0 is the (specular) reflectance when the surface is perfectly smooth. This relation holds for all values of σ /λ when the surface height distribution is Gaussian[21]. Experimentally, it has been shown [19] that ground glass (including Pyrex and fused quartz) has a Gaussian height distribution except for the most finely ground surfaces. And even the most finely ground are approximately Gaussian at small values of σ /λ.

The required values of σ/λ are given in Table 2-3 for specified values of relative specular reflectance R_s/R_0 at normal incidence.

Table 2-1 Directional Emissivity of UHV Aluminum

x	$\epsilon(x)$	x	$\epsilon(x)$
0	0.009701	0.62	0.010841
0.02	0.009702	0.64	0.020974
0.04	0.009703	0.66	0.011124
0.06	0.009706	0.68	0.011292
0.08	0.009710	0.70	0.011483
0.10	0.009715	0.72	0.011700
0.12	0.009721	0.74	0.011948
0.14	0.009729	0.76	0.012233
0.16	0.009738	0.78	0.012565
0.18	0.009748	0.80	0.012956
0.20	0.009761	0.82	0.013421
0.22	0.009775	0.84	0.013984
0.24	0.009792	0.86	0.014678
0.26	0.009810	0.88	0.015559
0.28	0.009831	0.90	0.016715
0.30	0.009854	0.92	0.018313
0.32	0.009880	0.94	0.020695
0.34	0.009908	0.96	0.024750
0.36	0.009940	0.98	0.033961
0.38	0.009976	0.99	0.046836
0.40	0.010015	0.999	0.130358
0.42	0.010058	0.9999	0.273129
0.44	0.010106	0.99995	0.301789
0.46	0.010158	0.99996	0.306524
0.48	0.010217	0.99997	0.308839
0.50	0.010281	0.99998	0.304665
0.52	0.010352	0.99999	0.279402
0.54	0.010430	0.999999	0.136803
0.56	0.010517	1	0
0.58	0.010614		
0.60	0.010721		

Table 2-2 Partial Hemispherical Emissivity of UHV Aluminum

c	$\epsilon \, (\Delta x)$	c	$\epsilon \, (\Delta x)$
0	0.012941	0.26	0.014068
0.02	0.013008	0.28	0.014186
0.04	0.013076	0.30	0.014310
0.06	0.013148	0.32	0.014441
0.08	0.013223	0.34	0.014578
0.10	0.013301	0.36	0.014724
0.12	0.013382	0.38	0.014877
0.14	0.013467	0.40	0.015040
0.16	0.013556	0.42	0.015212
0.18	0.013649	0.44	0.015396
0.20	0.013747	0.46	0.015590
0.22	0.013848	0.48	0.015796
0.24	0.013955	0.50	0.016020

Table 2-3 Surface Quality Required For Specified Specularity

R_s/R_O	σ/λ
0.99	0.00798
0.98	0.01131
0.97	0.01389
0.96	0.01608
0.95	0.01802
0.94	0.01979
0.93	0.02144
0.92	0.02298
0.91	0.02444
0.90	0.02583
0.80	0.03759
0.70	0.04753
0.60	0.05688
0.50	0.06625
0.40	0.07617
0.30	0.08732
0.20	0.10095
0.10	0.12075
0.05	0.13773
0.02	0.15739
0.01	0.17077

At non-normal incidence to a first approximation, σ is replaced by $\sigma \cdot \cos \theta$ where θ is the incidence angle with respect to the surface normal (3).

The non-specular reflectance pattern is not diffuse in the sense that the radiance is independent of θ. For normal incidence, the fraction of non-specular (called incoherent in[20]) radiation that is scattered into an angle between θ and $\theta + d\theta$ is given by

$$\gamma_d(\theta) = R_o \cdot 2\pi^4 \cdot (a/\lambda)^2 \cdot (\sigma/\lambda)^2 \cdot (1 + \cos \theta)^4 \cdot \sin \theta$$

$$x \exp \left[-(\pi a \sin \theta/\lambda)^2 \right] \cdot d\theta$$

where a is the autocovariance length or correlation distance. If m is the root mean square slope of profile of the surface, it can be shown that ([18] Appendix)

$$a = \sqrt{2} \, \sigma/m$$

For small values of σ/λ, the exponential in the equation for $\gamma_d(\theta) \cdot d\theta$ is unity, and the angular dependence is given by $(1 + \cos \theta)^4 \cdot \sin \theta$. The normalized values of this function are plotted in Figure 2-1 together with those for a diffuse reflector ($\sin \theta \cdot \cos \theta$). The difference between the curves is not large. The solid dots show the normalized values of $\gamma_d(\theta) \cdot d\theta$ for $\sigma/\lambda = 0.1$ ($R_S/R_o \approx 0.2$) and $m = 1$. Increased surface roughness increases the relative non-specular reflectance at small angles to the surface normal (for normal incidence).

The adverse effect on a radiant cooler of even a small amount of diffuse reflection was discussed earlier. This effect apparently extends to other geometries. For example, Feldmanis[23] found that it was not necessary to consider specularly reflecting surfaces or to use a complex formulation in the thermal analysis of a space vehicle, but that experimental measurements agreed best with a simple diffuse model. The same held for the plane-parallel and perpendicular plate geometries studied by Viskanta, et. al.[22]. Even for R_S/R_o in the range from 0.75 to 0.38, the measured distribution of radiant incidence across the surfaces agreed best with the simple diffuse model. One of the samples studied had a surface of smooth electroplated gold with $\sigma/\lambda \approx 0.007$, which should be highly specular ($R_S/R_o \approx 0.99$). The measurements were compared only with the simple diffuse and non-directional specular models; they agreed better with the diffuse. No explanation was offered for this, but Figure 15 of the report indicates that a directional specular model (i.e., including the emissivity as a function of θ) would account for most of the difference between the simple specular model and the experimental data. Unfortunately, directional specular calculations were not made for the smooth gold sample.
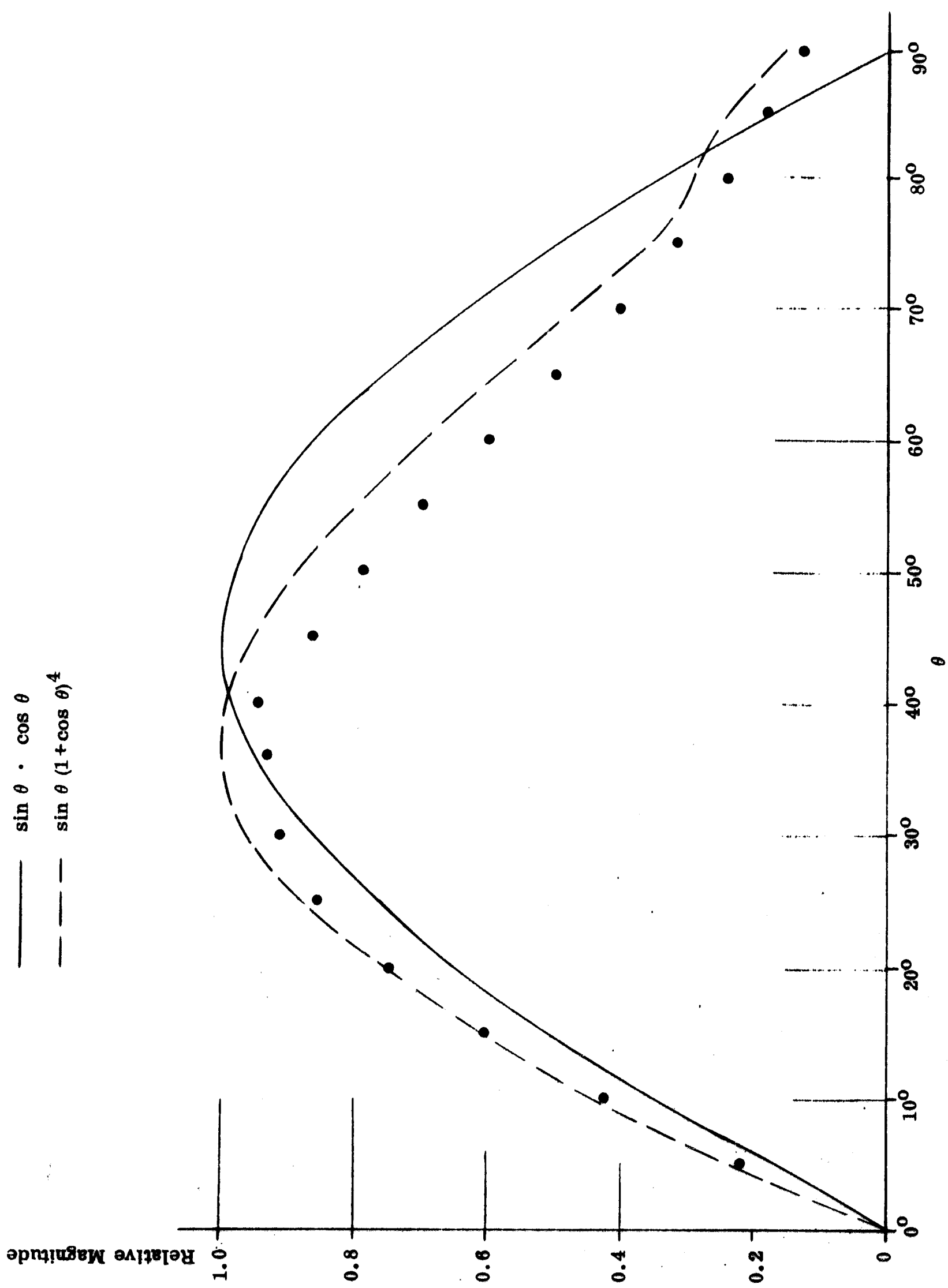
Figure 2-1 Reflectance Distribution Curves

—— $\sin \theta \cdot \cos \theta$

– – – $\sin \theta \, (1 + \cos \theta)^4$

In order to obtain the desired value of R_s/R_0 the surface roughness must be related to the surface optical deviations. If a Gaussian height distribution of surface irregularities is assumed, σ is related to the maximum (peak-to-peak) surface irregularity σ_{pp} by[24]

$$\sigma = \frac{\sigma_{pp}}{2\sqrt{2}}$$

The measurement of σ_{pp} by means of multiple beam fringes of equal chromatic order is described by Dietz and Bennett[24].

Now the cone radiates as an approximate greybody with a representative wavelength of 20 μm. The fraction p of greybody radiation beyond 20 μm is given in Table 2-4 for the usual range of cone wall temperatures T_c.

Table 2-4 Fraction of Cone Wall Radiation Beyond 20 μm

Tc (K)	p ($\lambda > 20\,\mu$m)
200	0.518
190	0.555
180	0.595
170	0.637
160	0.681
150	0.725

We will use values of σ/λ at $\lambda = 20\,\mu$m as the measuring point for cone wall roughness. Since surface deviations are usually measured in the visible using sodium light at a wavelength λ_{vis} of $0.5893\,\mu$m, we need to know the corresponding irregularity $\sigma_{pp}/\lambda_{vis}$:

$$\frac{\sigma_{pp}}{\lambda_{vis}} = 2 \cdot \sqrt{2} \cdot \frac{\sigma}{\lambda} \cdot \frac{\lambda}{\lambda_{vis}} = 96.65 \frac{\sigma}{\lambda}$$

The visibly measured surface irregularity corresponding to a specified reflectance ratio R_s/R_0 at 20 μm is given in Table 2-5.

Table 2-5 Required Surface Irregularity in the Visible
For Specified Specularity at 20 μm

R_s/R_0 (20 μm)	$\sigma_{pp}/\lambda_{vis}$ (wavelength)
0.99	0.77
0.98	1.09
0.97	1.33
0.96	1.54

A surface polished to be flat will have an irregularity of about 1/5th to 1/10th its deviation from flatness. Therefore, a surface having an irregularity of 0.77 wavelength must be flat to within 3.85 to 7.7 wavelengths (7.7 to 15.4 fringes).

Rather than specify the surface irregularity (which determines R_s/R_o), we could specify the flatness as measured on the polishing block. The sphericity (overall surface curvature) introduced upon remlval from the polishing block is no problem and should not change the irregularity. An on-the-block flatness of I wavelength (of visible light) would then ensure an R_s/R_o value of greater than 0.99 at wavelengths of 20μm and larger. In addition, it should be noted that a ratio 0.99 at 20μm at normal incidence results in the same ratio at 10μm when radiation is incident at 60° from the surface normal.

2.3 References

1. R. V. Annable, R. A. Harber, and H. A. Leiter, First Quarterly Report (Design Study Report) For a Day-Night High Resolution Infrared Radiometer Employing Two-Stage Radiant Cooling, Contract NAS5-10113, May 1966, Appendix II.

2. R. V. Annable, et. al., Final Report For a Day-Night High Resolution Infrared Radiometer Employing Two-Stage Radiant Cooling, Part I, Contract NAS 5-10113.

3. W. H. Wallschlaeger, et. al., Final Report, Development of a Single Stage Radiant Cooler For the ITOS VHRR, Contract NAS5-10491 (Mod. 12), June 1970, p. 3-13.

4. R. V. Annable, Final Report For Radiant Cooler Design and Emissivity Study, Part II, December 1969, Section 3.0.

5. R. V. Annable, Appl. Opt. 9, 185, 1970.

6. M. Jakob, Heat Transfer, Vol. II, John Wiley, 1957.

7. ASTME Tool Engineers Handbook, McGraw-Hill, 1959, Section 89.

8. E. M. Sparrow and R. D. Cess, Radiation Heat Transfer, Brooks/Cole, 1966, Section 2.3.

9. H. C. Hottel and A. F. Sarofim, Radiative Transfer, McGraw-Hill, 1967.

10. F. Seitz, The Modern Theory of Solids, McGraw-Hill, 1940, p. 638.

11. H. E. Bennett, M. Silver, and E. J. Ashley, Jour. Opt. Soc. Am. 53, 1089, 1963.

12. Reference 9, Section 4.10.

13. J. M. Bennett and E. J. Ashley, Appl. Opt. 4, 221, 1965.

14. R. B. Scott, Cryogenic Engineering, D. Van Nostrand, 1959, Section 10.15.

15. V. E. Holt, R. J. Grosh and R. Geynet, Bell Sys. Tech. Jour. 41, 1865, 1962.

16. M. Jakob, Heat Transfer, Vol. I, John Wiley, 1949, pp 34-52.

17. H. Davies, Proc. Inst. Elec. Engrs. 101, 209 (1954).

18. H. E. Bennett and J. O. Porteus, Jour. Opt. Soc. Am. 51, 123 (1961).

19. H. E. Bennett, Jour. Opt. Soc. Am 53, 1389 (1963).

20. J. O. Porteus, Jour. Opt. Soc. Am. 53, 1394 (1963).

21. P. Beckmann and A. Spizzichino, The Scattering of Electromagnetic Waves from Rough Surfaces, Pergamon Press, Inc., New York, 1963.

22. R. Viskanta, J. R. Schornhorst, and J. S. Toor, Analysis and Experiment of Radiant Heat Exchange Between Simply Arranged Surfaces, AFFDL-TR-67-94, Wright-Patterson AFB, Ohio, June 1967.

23. C. J. Feldmanis, Thermal Test of a Model Space Vehicle, Part II - Experimental Results and Comparison with Analysis, AFFDL-TR-67-42, Wright-Patterson AFB, Ohio, August 1968.

24. R. W. Dietz and J. M. Bennett, Appl. Opt. 5, 881 (1966).

3.0 ANTI-FROST DESIGN

The structure and operation of the radiant cooler must be designed to minimize the condensation of water vapor and other contaminants on optical components and sensitive cooler surfaces. To begin with, the compartments within the cooler are sealed from each other and from the instrument housing. For this purpose, windows are placed on the optical ports connecting the housing with the cooler and the cone enclosure with the patch enclosure (Section 3.3). Next, each cooler compartment (the cone compartment between the housing and outer cone structure and the patch compartment between the cone structure and patches) must be efficiently outgassed prior to cooler operation. Thirdly, the optical ports must be protected against contamination by residual internal outgassing products and by the ambient spacecraft atmosphere. Finally, provision must be made for driving off contaminants accumulated on the optics or on sensitive cooler surfaces.

To accomplish the initial outgassing, cooler operation is delayed by means of a cover over the cone mouth (Section 6.2 of the design study report) and by heaters on the cone walls and patches. If possible, the heaters should raise the cooler temperature to above ambient. A 10% change in absolute temperature changes the outgassing rate by about 10:1, according to Scialdone and Viehmann (Report of the Findings of the Radiation Cooler Task Group, Appendix VI, Sept 11, 1970). Thus, a temperature of 55°C, or about 10% above room temperature on an absolute scale, would be desirable. The patch temperatures, of course, should not exceed the limit set by the detector elements (about 80°C for HgCdTe). The structure should also provide paths for outgassing to outside the instrument. Thus, the multilayer insulation in both compartments will be perforated together with the outer mechanical structure of the cone and patch compartments. After a certain time interval, the materials within the cooler compartments will reach their steady-state or residual outgassing (weight loss) rates. Materials with low residual rates should therefore be used and the surface area of the multilayer insulation kept as small as possible consistent with the thermal insulation requirements.

With the cooler at its operating temperatures, both the internal residual outgassing and the ambient spacecraft atmosphere are sources of contaminants. The cooler should then be designed to keep deposits off the optical ports on both the patches and cone structure. A cold surface in the vicinity of the optical openings on the patches can be used to trap moisture before it reaches the windows. These traps also serve to divert the gas flow away from the patch opening during the initial outgassing period prior to cooler operation. Baffles can be used to block the flow of residual insulation outgassing products to the optical ports. The cold traps and baffles will be used in place of the anti-frost enclosure (Section 6.3 of the design study report).

In support of this approach, tests performed on Contract NAS5-21112 (SCMR for Nimbus E) have shown that a polyimide antifrost enclosure acts as a (conductive and radiative) condenser to significantly increase the radiative input through the optical opening from the cone (window) to the patch. The enhancement of radiative coupling was observed during the testing of the enclosure and during the testing of a breadboard model of the SCMR cooler. In the first case, a 220°C blackbody at a fixed distance was

viewed through a chopper by a cooled PbSe detector. Insertion of the enclosure (including an infrared window) increased the detector signal from the blackbody. In the second case, the insertion of two enclosures produced a thermal input sufficient to increase a 100K SCMR cooler patch to 125K. This was true even when a thin section was removed from each enclosure next to the cone in order to disconnect its conductive paths. There were no spectral filters or germanium windows on the patch during these tests, only black openings. Addition of the germanium should reduce the higher temperature to 117K, still a very large increase. Apparently, the inside of the enclosure would have to be blackened to eliminate the condenser effect. This would, of course, increase the conductive radiative coupling through the enclosure.

Finally, the operation of the instrument may eventually be impaired either thermally or optically by the accumulation of frost or other contaminants. Cooler operation is then interrupted by closing the cone cover and reheating the cone and patches to drive off the condensed material. A successful anti-frost design would be one in which the time between such interruptions is large, say a significant fraction of the instrument's orbital lifetime.

The initial and residual outgassing of the insulation below the patches are studied in Section 3.1. The study indicates that patch contamination from this source should not be a problem if the patch compartment is sealed from the rest of the instrument and well outgassed prior to operation of the cooler. A literature review on the subject of multilayer insulation is discussed in Section 3.4. The construction of the patch cold traps and insulation baffles are covered in Section 3.2.

A proper test of the anti-frost design of a radiant cooler can be carried out in a space chamber with respect to the initial outgassing and the contamination produced by residual internal outgassing. Procedures used during the test must be realistic in the sense that they can also be followed in orbit. A proper test with respect to contamination produced by the spacecraft atmosphere is considerably more difficult. It would require the exposure of a cooler to the expected pressures and constituents before and after initiation of cooler operation. During cooler operation, the correct temperatures' would have to be maintained not only on the patches but also on the other cooler parts without the presence of cold space targets and shrouds in the immediate vicinity of the cooler.

Previous tests have shown that it is possible to design and operate a radiant cooler so that water vapor or other contaminants from the vicinity of the patch do not impair its operation. For example, extensive testing of radiant coolers for the ITOS-VHRR (patch temperatures of 85 to 100K; Contract NAS5-10491) has never revealed any evidence of ice on the detector optics sufficient to degrade the sensitivity of the instrument. In this design, the detector is in a second-stage patch that is surrounded by a first-stage patch. The first-stage may then act as a simple cold trap for the second-stage. Moreover, the detector package is relatively distant from the major paths for gas leaving the space between the patch assembly and cone. structure.

In addition, the cone is sealed (by the spectral filter) from the rest of the instrument, so that outside outgassing products cannot pass by the cold patches. The chamber pressure is initially reduced to about 2×10^{-6} Torr (it is probably higher in the insulation blankets) and the cryopanels turned on. The final chamber pressure is typically 5×10^{-7} Torr. The operation should be improved further by heating the cooler parts (patches and cones) during pumpdown.

3.1 Outgassing of Patch Insulation

The volume below the patches in the multi-element radiant cooler is sealed from the rest of the cooler. As a result, instrument outgassing products that can condense on the patches must come from this volume. The source of outgassing is the multilayer insulation between the patch and the cone structure. If the insulation is allowed to out-gas at room temperature for a sufficient length of time prior to cooler operation, the residual outgassing rate will be so small that it will not degrade sensitivity for a long time. For example, we may begin with the data given by Scialdone and Viehmann for an as-received stack of insulation (Figure 3 to Apprendix VI of the LaGow Committee Report). If this stack is pumped for 1000 mins (16.7 hrs) and if the outgassing rate remains constant beyond that time, it is shown below that a 10% reduction in signal requires 170 to 230 days, depending on the wavelength. This result assumes that the outgassing product is water that is uniformly deposited as ice on the rear surfaces of the patches. If the stack is pumped for 2000 mins (33.3 hrs) or purged with helium at 100°C and pumped for 1000 mins. the time required for a 10% signal decrease is increased by a factor of 10. Moreover, the reduction in temperature of the insulation during cooler operation should greatly reduce the residual outgassing rate.

If G is the outgassing rate in torr-liters cm^{-2} sec^{-1} of equivalent air, the outgassing rate for water in gm cm^{-2} sec^{-1} is (Scialdone and Viehmann, op. cit.).

$$G \times 1.7 \times 10^{-3} \times 18/29 = 1.1 \times 10^{-3} \, G$$

There are about 30 layers (15 pairs) of multilayer in the main stack between the patches and cone structure. Each layer has an area of about 100 in^4 including the end pieces. Counting both sides of the layers, this is a total of 6×10^3 in^2. There is an additional small stack with a total (both sides) area of about 200 in^2 around the second patch. The total insulation surface area is then 6.3×10^3 in^2 or 4.0×10^4 cm^2. The total outgassing rate is then 44G grams of water per second.

We will assume that all of the outgassed water is deposited as ice or frost uniformly on the rear surfaces of the patches. The rear surfaces have an area of about 16.6 in^2 or 107 cm^2 (p. 4-2 of the design study report). Assuming a density of 1 gm cm^{-3}, the ice thickness then increases at the rate of 3.6×10^3 G cm day^{-1}.

For lack of data on the attenuation of infrared radiation by ice, we will use the values of liquid water (W. L. Wolfe in Handbook of Military Infrared Technology, Office of Naval Research, 1965, p. 363). The maximum extinction coefficient in the 1 to 3 μm band (where an InAs detector would be used) is 0.0680 at 3.00μm, and the maximum in the 8 to 12.5μm band (where a HgCdTe detector would be used) is 0.2438 at 12.5μm. The transmission through a water thickness δ is given by

$$T = \exp(-\alpha\delta) = \exp(-4\pi n k \delta/\lambda)$$

where α = absorption coefficient

   n = refractive index

   k = extinction coefficient

   λ = wavelength of radiation

Thus, for T = 0.90, we have

$$\delta(3\mu m) = 2.43 \times 10^{-5} \text{ cm}$$

$$\delta(12.5\mu m) = 3.34 \times 10^{-5} \text{ cm}$$

The refractive index of water is 1.446 at 3.00μm and 1.219 at 12.5μm.

For 1000 minutes of pumping on as-received insulation at 24°C, G is about 4×10^{-11} torr-liter cm^{-2} · sec^{-1} (Figure 4 of Scialdone and Viehmann). The ice thickness growth rate is then 1.44×10^{-7} cm per day. The times required to attenuate the signals by 10% are then

$$t(3\mu m) = 169 \text{ days}$$

$$t(12.5\mu m) = 232 \text{ days}$$

If the insulation is pumped for 2000 minutes or for 1000 minutes after a helium purge at 100°C, G is reduced by a factor of 10 and t increased by the same factor.

After the cooler has reached its operating temperature, the insulation will be considerably below room temperature. The reduction in temperature would be expected to reduce the outgassing rate. Scialdone and Viehmann state that a rule of thumb is a 10% change in absolute temperature changes the outgassing rate by 10:1. If this rule holds at temperatures down to the 90K to 170K range, there would be a large reduction in the residual outgassing rate. For example, the operating cone temperature of design IIIA is about 170K or 40% less than room temperature on an absolute scale.

We may therefore conclude that patch contamination by instrument outgassing should not be a problem if the volume between the patch and cone structure is sealed from the rest of the instrument and well outgassed prior to operation of the cooler. We hope to resolve the uncertainty about the attenuation coefficients by obtaining a copy of the dissertation on ice crystals referenced in Figure 5 of Appendix II enclosure 2 to the LeGow Report.

3.2 Anti-Frost Devices

The optical openings within the patch enclosure will be protected against frost by the simple cold traps and baffles shown in Figure 3-1. The traps and baffles are designed to divert flow away from the optical parts during initial and residual (steady-state) outgassing. The cold traps are designed to capture contaminants from both the residual internal outgassing and the ambient spacecraft atmosphere.

The cold trap on the upper (120K) patch is metallic and does not contact the insulation blanket. The cold trap on the lower (90K) patch is plastic and penetrates the insulation. However, the insulation temperature at the end of the plastic is the order of 120K or as cold as the upper patch. The inside of the metallic cold trap will be painted black. The plastic cold trap and the plastic insulation baffles may be either black or highly transmitting in the infrared. The black could be supplied by a paint or by included carbon particles. A suitable material in either case appears to be high-density polyethylene (see N.W.B. Stone and D. Williams, Appl. Opt. 5, 353, 1966 and J. M. Blea, et. al., Jour. Opt. Soc. Am. 60, 603, 1970).

Outgassing of the patch enclosure will be aided by performations in both the multilayer insulation and in the cone end that forms part of the patch enclosure.

3.3 Optical Port Design

The selection of windows for the optical ports on the cone and patches is discussed in Appendix B to the design study report (July 1970). The cone windows are used to essentially eliminate radiative coupling between the patch and warmer components beyond the cone in the direction of the instrument housing. They also provide mechanical seals for the volume between the patches and cone structure. The optical ports are sealed to prevent outgassing of the instrument and remainder of the cooler through the volume containing the patches.

The cone and patch windows will be the same for the optical ports to the 120K (InAs) patch and the 90K (HgCdTe) patch. The window materials are Intran 2 and germanium, respectively. A germanium window would probably not be used on the 120K patch in an actual instrument. The germanium does not transmit below about 2μm. However, its thermal performance is comparable to that of a sapphire window, so that it is satisfactory for thermal testing. In addition, the thermal input through the optical opening is not critical to the performance of the 120K patch.
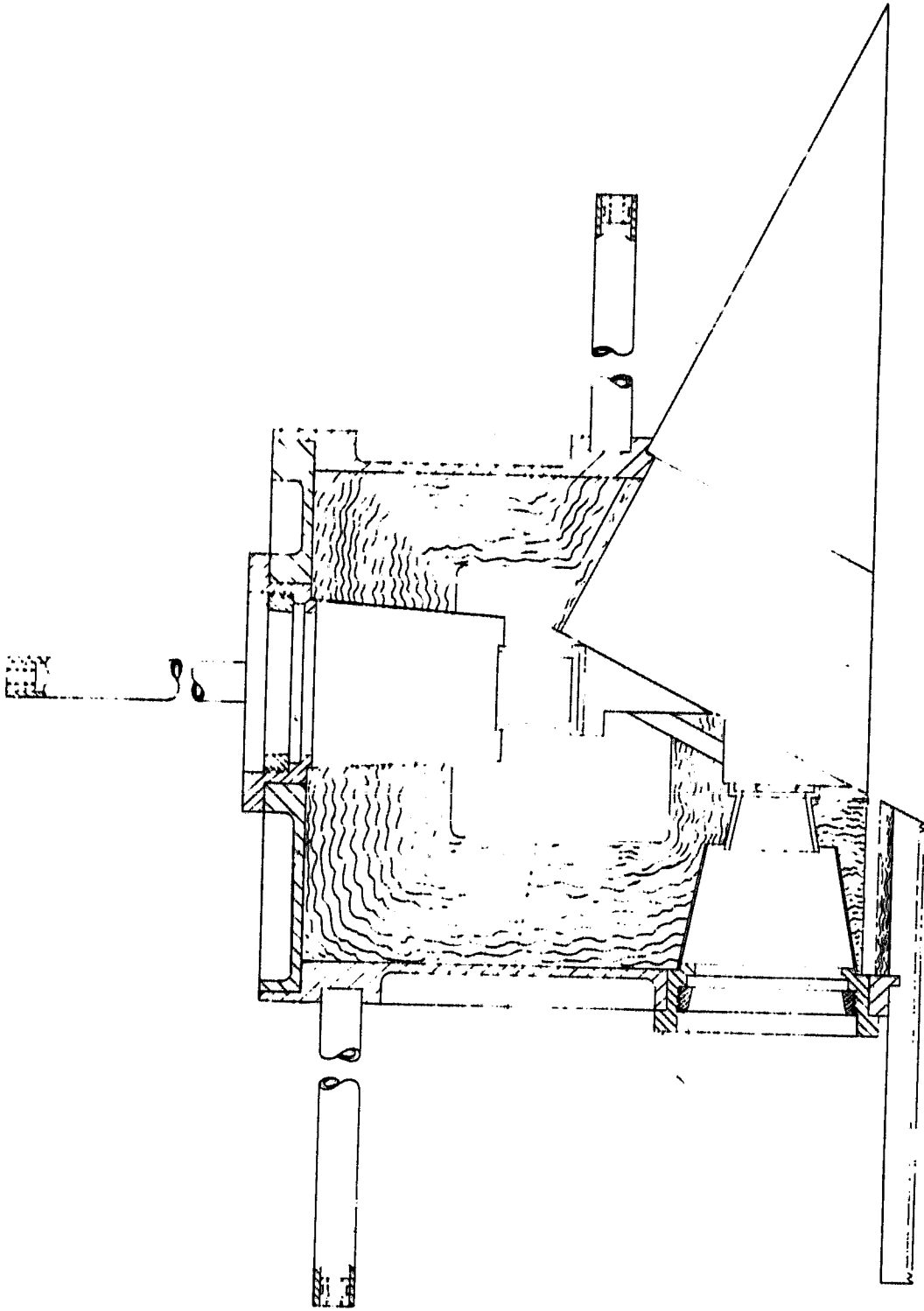
Figure 3-1 Anti-Frost Device

The Irtran 2 cone windows (Eastman Kodak Co.) are 1-inch in diameter and 2 mm thick. The germanium patch windows (Exotic Materials Inc.) are 0.5 inch in diameter and 1 mm thick. All windows have a commercial plate glass finish, 5 wavelengths per inch flatness, and 5 minutes of arc parallelism.

The clear aperture of each patch window will be 0.4 inch after mounting. The divergence angle ψ from the optic axis at the patch window will be based on

$$\tan \psi \approx 1/2 f_n = \phi D / 2 s$$

where f_n = f-number of optics at the patch window

ϕ = instantaneous geometric field of view

D = diameter of entrance aperture

s = side of a detector element sensitive area

For a typical instrument in the 120K channel,

ϕ_1 = 0.5×10^{-4}

D = 25.4 cm

s_1 = 1×10^{-2} cm

The resultant divergence is

$$\tan \psi_1 = 0.0635$$

To provide for mechanical clearances and tolerances, $\tan \psi_1$ was set at 0.070. In the 90K channel, we used the following values

ϕ_2 = 1.75×10^{-4}

D = 25.4 cm

s_2 = 1.5×10^{-2} cm

In this case, $\tan \psi_2 = 0.148$. Mechanically, a value of 0.150 will be used. The field-of-view ratio ϕ_2/ϕ_1 was set equal to the reciprocal of the detector element ratio (3.5), on the assumption that the channels have the same spatial coverage.

3.4 Multilayer Insulation - A Review

We conducted a review of some readily available literature on the subject of multilayer insulation. Some of the articles revealed that the problem of outgassing is not a new one. R.H. Kropschot (Multiple Layer Insulation for Cryogenic Applications, Cryogenics, March 1961, p. 171) discusses the measurement of the effective thermal conductivity of multilayer insulation without perforations or end effects. In his description of the experimental procedure, he states that

> "During evacuation, the sample temperature was maintained at approximately $100^{o}C$ for about 3 days to help drive the residual moisture from the sample."

J.W. Price (Measuring the Gas Pressure Within a High Performance Insulation Blanket, in Advances in Cryogenic Engineering, Vol. 13, Ed. by K. D. Timmerhaus, Plenum Press, 1968, p. 662) studied the effect of perforations on the performance of multilayer. We tested layers with 1/8 inch diameter holes on 1 inch centers in both directions (1.2% areal perforation). The holes were not aligned between layers. He states that

> "The (approximately) 1% ratio was chosen because analyses showed that this ratio is effective in increasing the evacuation rate and does not materially degrade the thermal efficiency of the insulation."

This was verified by his experiments. He also concludes that the insulation should be preconditioned by means of a vacuum pumpdown, dry gas purge, or both. Finally, he states that there is a problem with insulation evacuation and much of it is a result of material outgassing.

G. C. Vliet and R. M. Coston (Thermal Energy Transport Parallel to the Laminations in Multilayer Insulation, ibid., p. 671) conclude that the lateral conductivity through an insulation blanket depends on its temperature. They studied this effect in samples of crinkled mylar aluminized on one side (NRC-2). The data indicates that radiation transfer along the laminations can be significant and result in much higher parallel conductivity values near room temperature than predicted from conduction through the aluminum film. However, the lateral conductivity drops rapidly with temperature, and below about 100K the "size effect" of the aluminum film limits it to values less than that of the film. From this, we may conclude that radiation transfer along the lamina is important in the insulation of the cone from the instrument housing. When insulating the patches from the cone, however, the temperatures are in the transition region and such radiation "tunneling" is largely gone.

D. O. Murray (Degradation of Multilayer Insulation Systems by Penetrations, ibid., p. 680) discusses techniques for decoupling supports from the insulation blanket. An intermediary insulation (decoupler) is placed around the penetration. The optimum for his setup consisted of a decoupler space on all sides equal to the diameter of the support. Aluminized mylar radiation shields concentric with the support were placed within a concentric wrapping of dexiglas. Unfortunately, the dexiglas or any similar material is a good absorber of water and therefore undesirable. It may be possible to substitute dimpled mylar or other plastic film, possibly with an aluminum coating.

4.0 EXPERIMENTAL STUDIES

Experimental programs were begun for determining the thermal properties of multilayer insulation and low-emissivity, specular surfaces as they apply to radiant coolers. These programs were also used to develop and evaluate techniques for the application of multilayer insulation and the fabrication and processing of cone walls.

4.1 Multilayer Insulation

The insulation value of the multilayer may be expressed as a shielding factor s_i or an equivalent thermal conductivity k_i. The shielding factor is the reciprocal of the effective emissivity or radiative coupling coefficient. The two parameters are related by

$$(1/s_i)(T_h^4 - T_c^4) = (k_i/t_i)(T_h - T_c)$$

where T_h = Temperature of warm boundary

T_c = Temperature of cool boundary

t_i = Thickness of layer

The multilayer experiments were directed toward obtaining techniques and parameters applicable to insulation of the space between the housing and outer cone walls.

The thermal balance equation of the high-emissivity radiating plate in the first insulation test fixture (Figure 4-1) is

$$\epsilon_p \, \sigma A_p \, (T_p^4 - T_o^4) = K_c \, (T_b - T_p) + (\sigma A_p/s_i) \cdot (T_b^4 - T_p^4)$$

where ϵ_p = effective emissivity between plate and liquid nitrogen target

A_p = top radiating area of plate

T_p = temperature of plate

T_o = temperature of liquid nitrogen target

T_b = base temperature

K_c = thermal conductance between plate and base

s_i = shielding factor of multilayer insulation

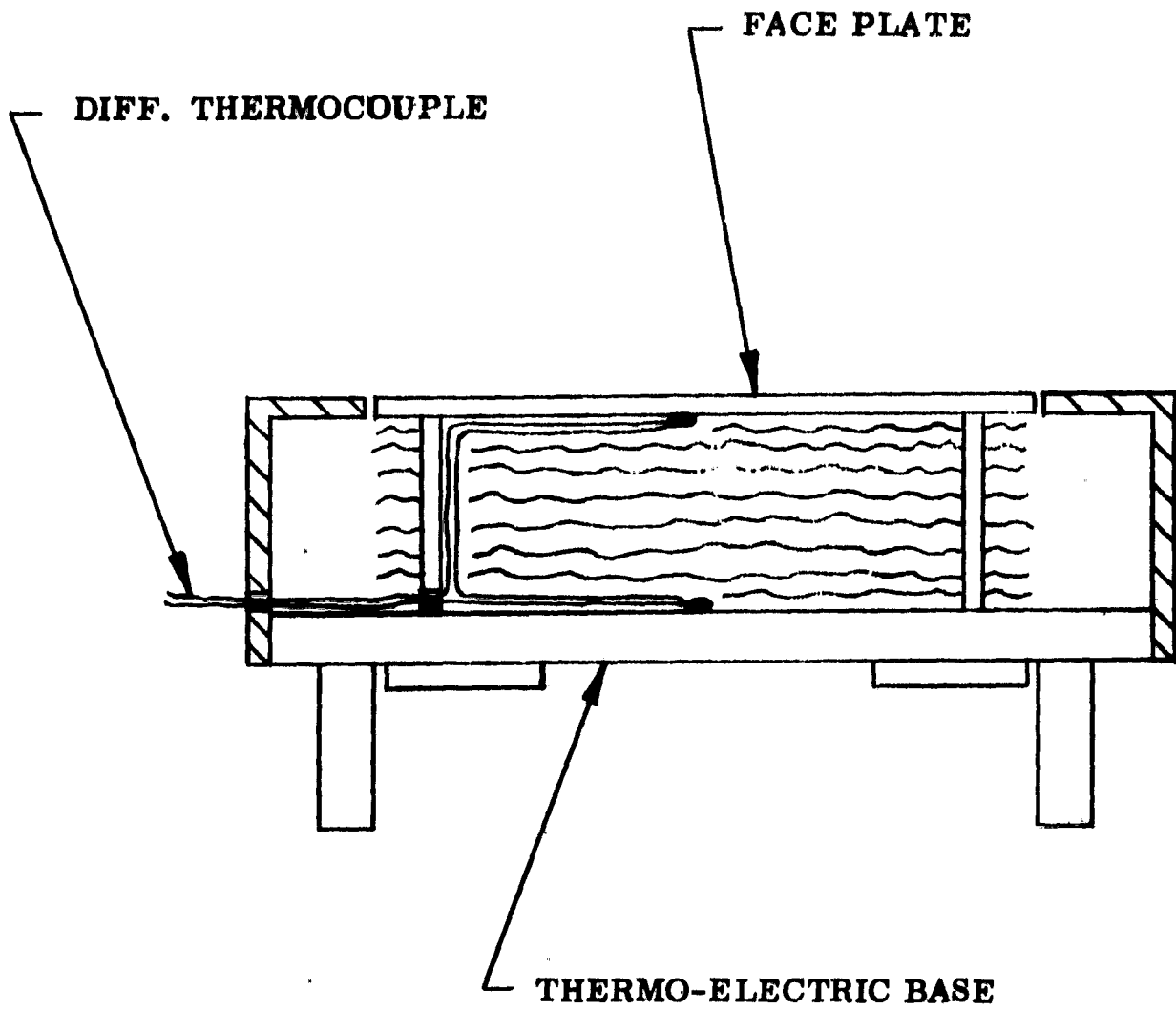DIFF. THERMOCOUPLE

FACE PLATE

THERMO-ELECTRIC BASE

Figure 4-1 Multilayer Insulation Test Apparatus

The plate is supported from the base by two fiberglass-reinforced epoxy tubes of 1/4 inch OD, 1/8 inch ID, and 1 inch length. The thermal conductivity of the material is about 3.5×10^{-3} W/cm° C. Including the effect of the nylon screws used for mounting, the supports have a thermal conductance of about 6.94×10^{-4} W/K. The thermocouple leads between the plate and base consist of one chromel wire and one constantan wire, each of 5×10^{-3} inch diameter and 1 inch length. These have thermal conductivities of 0.13 and 0.23 W/cm°C, respectively, and contribute a total conductance of 0.18×10^{-4} W/K. The value of K_c is therefore approximately 7.12×10^{-4} W/K.

For $\epsilon_p = 0.84$ (Section 4.2) and $A_p = 40$ in^2, the thermal balance equation then yields

$$1/s_1 = 0.84 \left(T_p^4 - T_o^4 / T_b^2 - T_p^4 \right) - 4.867 \times 10^5 \left(T_b - T_p / T_b^4 - T_p^4 \right)$$

An initial series of three tests were run. In the first two, a 1 inch blanket of multilayer was simply stacked below the plate, as shown in Figure 4-1. The blanket consisted of alternate layers of smooth and dimpled aluminized mylar sheets. The open ends of the blanket viewed a machined, but unanodized, aluminum surface. For the first test, there were 17 smooth and 16 dimpled sheets. The final (equilibrium temperatures were

$$T_o = 94 \text{ K}$$

$$T_p = 151 \text{ K}$$

$$T_b = 298 \text{ K (regulated)}$$

and the resultant shielding factor

$$s_i = 25$$

For the second test, the number of insulation sheets was increased by about 50%. However, this increased the shielding factor by less than 1%.

For the third test, the side walls seen by the open ends of the insulation blanket were covered by a smooth layer of insulation followed by a dimpled layer and a second smooth layer. The final temperatures were

$$T_o = 94 \text{ K}$$

$$T_p = 134 \text{ K}$$

$$T_b = 298 \text{ K}$$

and the resultant shielding factor

$$s_i = 60$$

The nature of the surface seen by the open ends of the insulation blanket therefore has a very large influence on the effectiveness of the multilayer. The ends apparently act as a black receiver whose radiative input is efficiently conducted down the aluminum film on the insulation sheets. (See Figure 3.4.) Because of the importance of the open ends, the test fixture was modified to more accurately represent an actual cooler cone. The ratio of blanket end area to insulated zone wall area is about 0.65 in the initial insulation test fixture. On the other hand, the ratio in a typical cooler is only 0.25. The insulated area was therefore increased by attaching a box to the underside of the plate. (Figure 4-2.) This modification has the additional advantage of reducing the influence of thermal conductance through the support tubes and thermocouple wires.

A series of tests were run with the modified multilayer insulation test fixture. The thermal balance equation of the high-emissivity plate in the new arrangement (Figure 4-2) is

$$\epsilon_p \, \sigma A_p \, (T_p^4 - T_o^4) = K_C \, (T_b - T_p) + (\sigma A_i / s_i) \cdot (T_b^4 - T_p^4)$$

where ϵ_p = effective emissivity between plate and cold space = 0.89

A_p = top radiating area of plate = 40 in^2

T_p = temperature of plate

T_o = temperature of cold space target

T_b = base temperature

K_c = thermal conductance between plate and base = 3.34×10^{-4} W/K

A_i = insulated area at T_p = 103 in^2

s_i = shielding factor of multilayer insulation

The flat plate faced a honeycomb cold target in this set of experiments. The emissivity of the paint (and therefore also of the plate) is about 0.91 (Section 4.2). The length to diameter ratio of the honeycomb cavities is sufficiently large that the limiting value of hemispherical emissivity is attained (See E. M. Sparrow and R. D. Cess, Radiative Heat Transfer, Brooks/Cole 1966, p. 165). The emissivity of a cavity may be estimated from the results of Sparrow or calculated from the formula of Treuenfels (Jour. Opt. Soc. Am. 53, 1162, 1963). The result is 0.977 for a paint emissivity of 0.91. About 8.2% of the space target is flat and remainder cavities. Its average emissivity is therefore 0.972, and the effective emissivity between the plate and target is about 0.89.
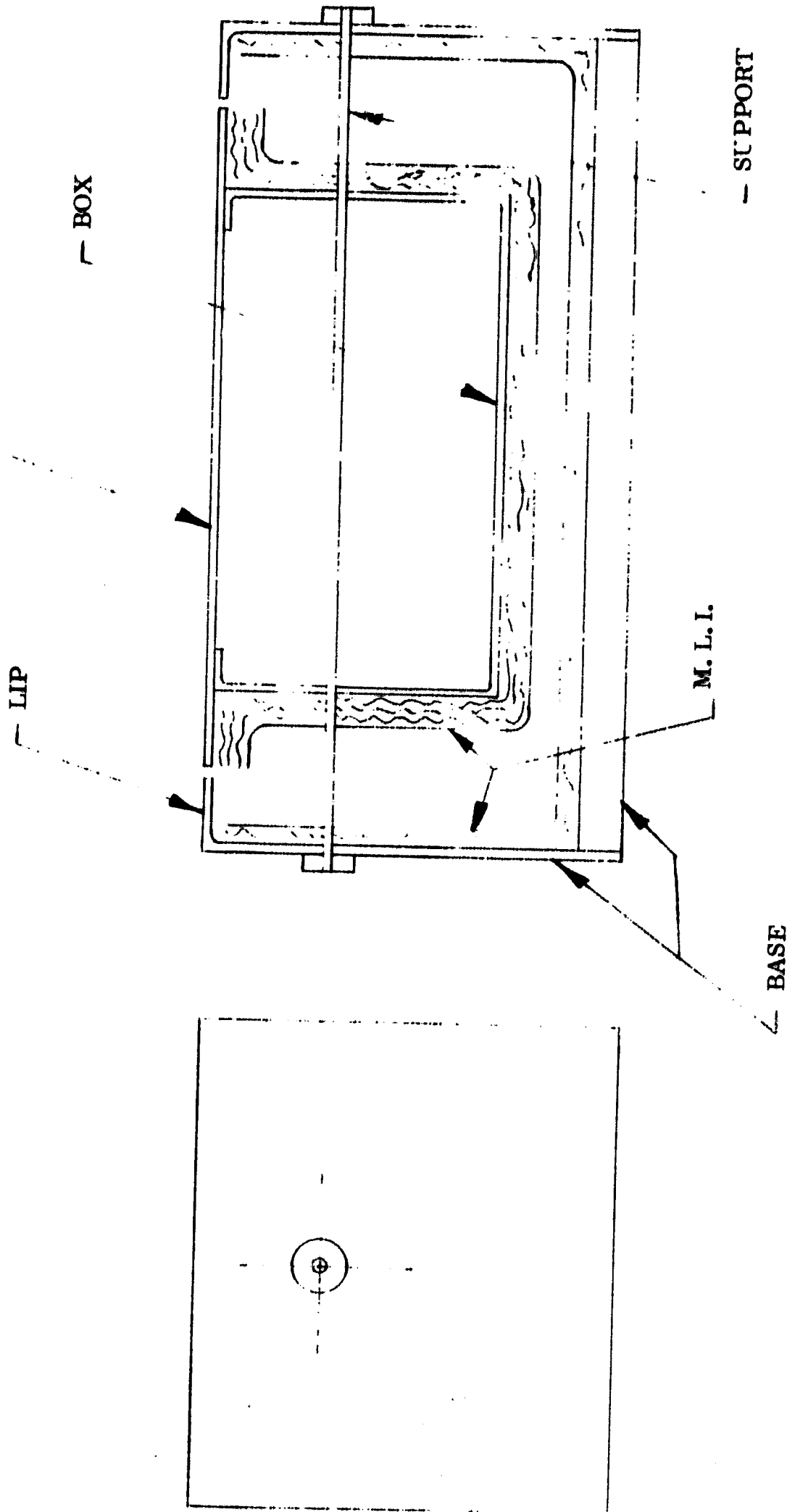
LIP

BOX

SUPPORT

M. L. I.

BASE

Figure 4-2 Multilayer Insulation Test Fixture Modification 1

The plate is supported from the base by two synthane tubes of 1/4 inch OD, 1/8 inch ID, and 1.89 inch length. The thermal conductivity of the material is about 3.3×10^{-3} W/cm · K and the thermal conductance of the supports, 3.265×10^{-4} W/K. The remainder of the conductance is produced by the thermocouple leads to the plate.

The tests run are listed in Table 4-1. For the first test, smooth sheets of aluminized mylar were attached to the inside of the base and the outside of the box, including the adjacent inside plate area. The results are given in Table 4-2. The theoretical improvement for perfect radiation shields, when the number of shields is increased from n_1 to n_2, is $n_2 + 1/n_1 + 1$. This ratio and the actual improvement are also shown in Table 4-2.

Table 4-1 Multilayer Insulation Tests in Modified Fixture

Test No.	Pairs* of Insulation on	
	Base	Box
1	0	0
2	0	2
3	0	4
4	2	4

* One pair is a smooth and a dimpled layer of mylar aluminized on both sides.

Table 4-2 Results of Insulation Tests

Test No.	T_o	T_p	T_b	s_i	Improvement Actual	Ideal
1	27.8	164.4	298.7	30.1	-	-
2	28.0	148.0	293.4	45.4	1.51	3
3	28.0	144.0	294.4	52.5	1.16	1.67
4	40.9	139.7	291.0	58.0	1.10	1.40

Following the fourth test, an additional 7 pairs were added to the base. This, however, increased s_i by only 1.18X (to 68.4) compared with an ideal of 2X. The open ends of the blanket on the base viewed the lip (Figure 4-2), which was covered with low-emissivity tape. We had previously demonstrated that such an arrangement degrades insulation performance. As a result, the lip will be removed and the plate

extended to within a small distance of the sides of the base. Except for one pair on the base, the multilayer will then be attached to the box and underside of the plate. This second modification more nearly duplicates the insulating of a cone in a typical radiant cooler.

4.2 Preliminary Estimate of Effective Cone Wall Emissivity

Previous experimental measurements have shown that techniques and materials used to prepare inner cone wall surfaces result in a low value (< 0.02) for the hemispherical emissivity (Final Report on Contract No. NAS5-11683, Part II, 8 April – 15 December 1969). These measurements, however, did not include any indication of deviations from specular reflectivity at the surface. Such deviations increase the apparent specular surface emissivity (ϵ_c).

A cooler cone of simple geometry was therefore designed for the purpose of obtaining a measure of the (effective) cone wall emissivity that includes the influence of deviations from specular reflectivity. Although the values obtained will strictly apply only to the exact cone geometry employed in the experiment, they will provide a direct and meaningful comparison between various cone wall surfaces. Photographs of one of the test cones are shown in Figures 4-3 and 4-4. Figure 4-3 shows the insulation box and support enclosure mounted below the cone. The polished, hardcoated aluminum inner surfaces are shown in Figure 4-4. The hardcoat is obtained by means of an anodic oxidation process.

A second test cone was constructed of optically polished, electroless nickel plated aluminum. The polished walls were covered with evaporated aluminum. This surface has been advocated as an inner cone wall surface by several workers, including those at A.D. Little, Inc. (F. Gabron, "Design Study of Passive Detector Cooling Techniques", Final Report on Contract NAS5-21009, August 29, 1969). The average surface flatness of the nickel-plated walls was about 17 wavelengths of visible light.

The value of ϵ_c was about 0.048 for both vacuum aluminized hardcoated aluminum and vacuum aluminized electroless nickel-plated aluminum. The results must be considered preliminary estimates for at least two reasons:

a.   The coupling between the rear of the patch and the cone structure was large in comparison with the coupling between the cone walls and the (black) front of the patch.

b.   The space target had a relatively high reflectivity that produced an undesirably large coupling between the walls and patch by way of the target.
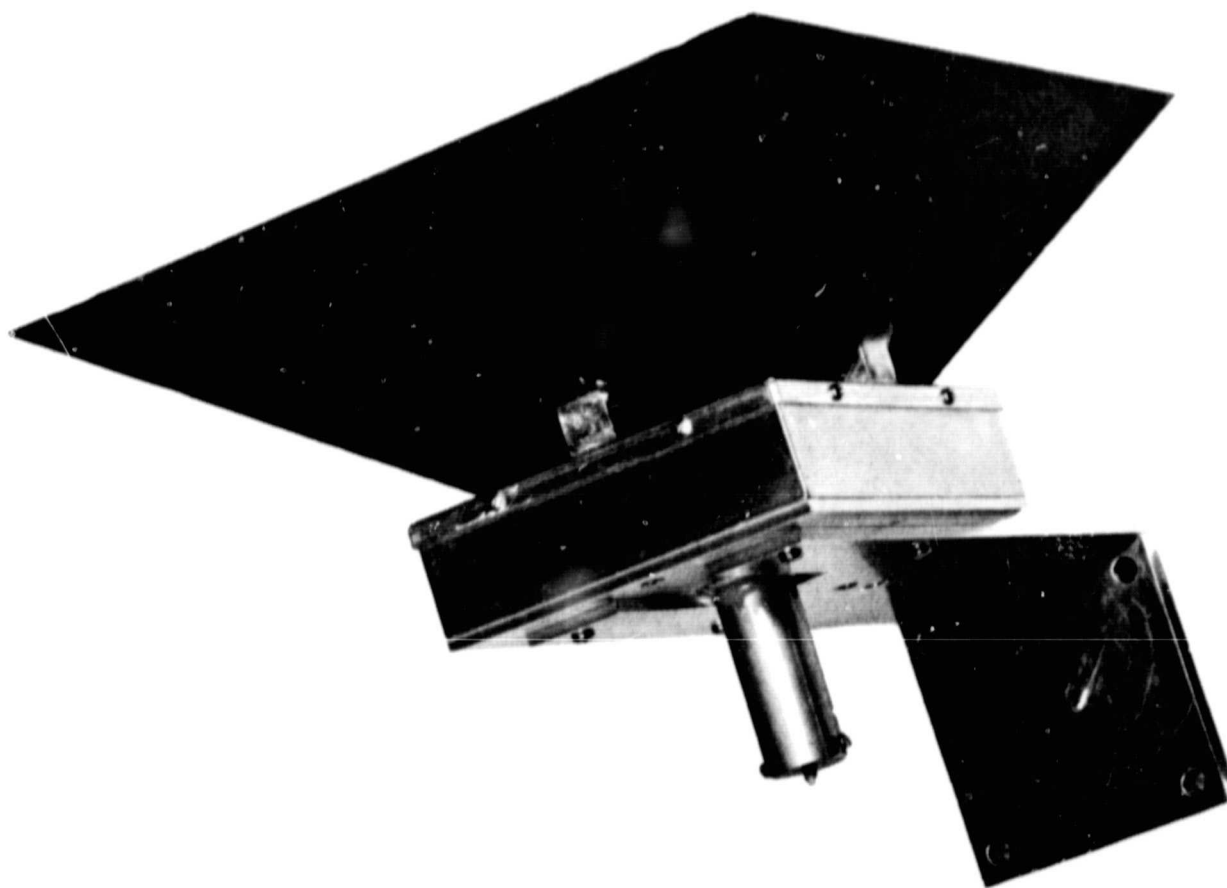
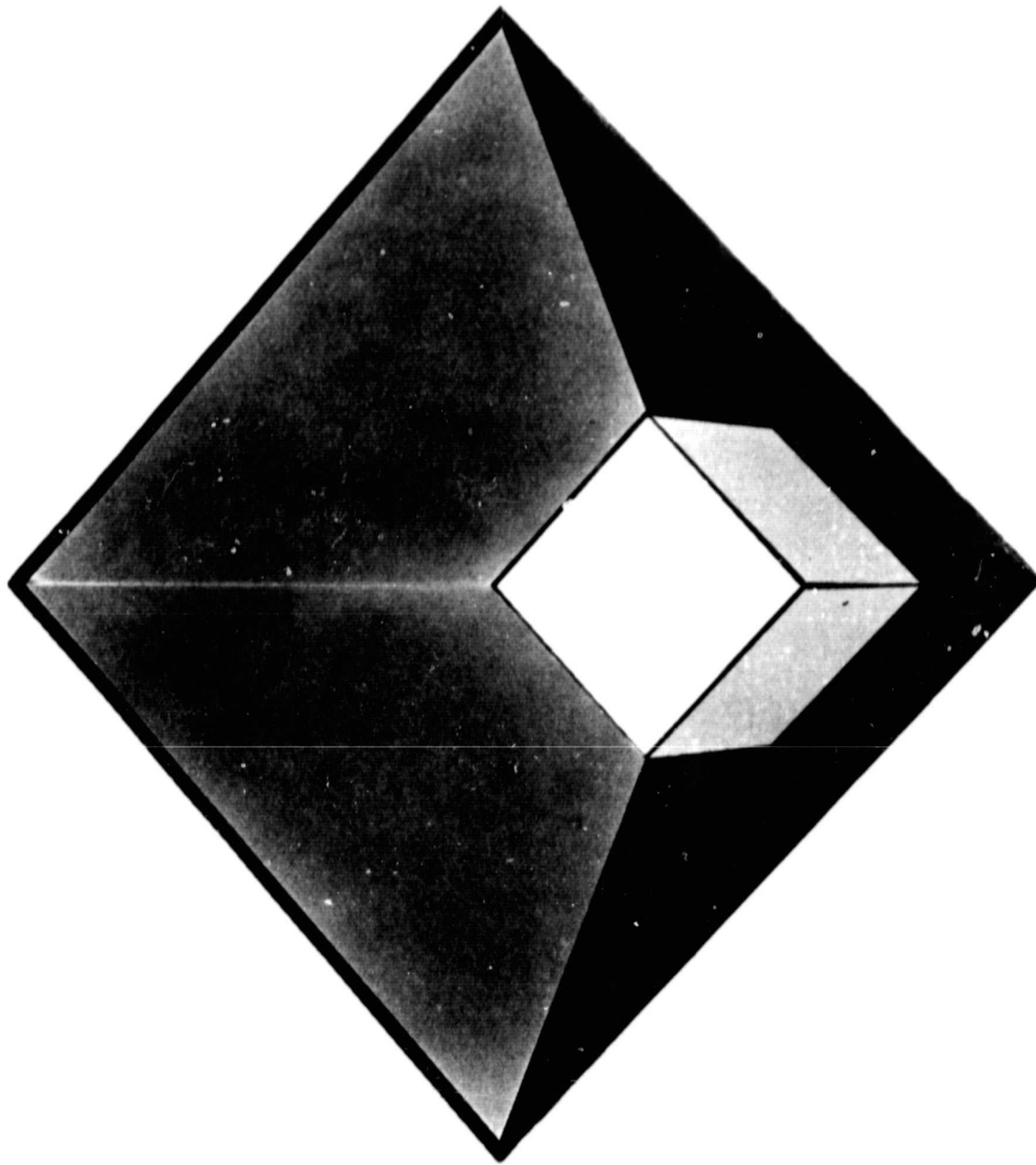Figure 4-3 Insulation Box and Support Enclosure

Figure 4-4 Polished, Hard Coated Aluminum Inner Surfaces of Cone

In spite of (a), the values determined for ϵ_c were quite consistent among several experiments run, especially for the hardcoated walls. This is a direct result of the apparently high accuracy (at least, repeatability) in the determination of both the coupling to the back of the patch and the effective emissivity for the patch to space target radiative interchange. Because of (b), the results must also be considered upper limits on the value ϵ_c. Repeating the test with a lower reflectivity space target should reduce the value of ϵ_c determined by means of the thermal balance equations.

The space target surface is an array of pyramids (two sets of v-grooves cut at right angles to each other). It may be considered an early (circa 1960) model in the development of satellite-borne radiometer technology. The array has little cavity enhancements. Moreover, the pyramid points are difficult to paint. The target will be replaced by a homeycomb cavity array attached directly to the liquid nitrogen reservoir by means of copper-filled epoxy.

The insulation below the patch is a simple stack of multilayer. It was designed for good outgassing properties. However, it has a large ratio of open end area (effectively black sides) to insulated area. This has previously been shown to be a poor arrangement from the standpoint of thermal isolation (Section 4.1). We should do better with a simple closed spaced geometry of low-emissivity surfaces between the rear of the patch and the cone structure and low-emissivity shields concentric with the two patch supports. After the modifications to the target and patch insulation have been completed, the cone tests will be repeated.

4.2.1 Test Results

The thermal balance equation of the patch in the test cone fixture is given by (assumes specular cone wall reflection)

$$\sigma \epsilon_p A_p (T_p^4 - T_o^4) = \sigma \epsilon_p^4 A_p \epsilon_{pc} (T_c^4 - T_o^4)$$

$$+ (\sigma A_i / s_i)(T_c^4 - T_p^4) + K_p (T_c - T_p) + \phi_h \qquad (4-1)$$

where ϵ_p = effective emissivity for radiative exchange between patch and space target

ϵ_{pc} = effective patch-to-cone emissivity

A_p = black radiating area of patch

A_i = rear and side area of patch insulated from the cone structure

T_p = patch temperature

T_o = space target temperature

T_c =   cone temperature

s_i =   shielding factor of insulation

K_p =   thermal conductance of supports and electrical leads

ϕ_h =   patch heater power

The effective cone-to-patch emissivity is related to the effective specular cone wall emissivity by

$$\epsilon_{pc} \;=\; F_{pc} \cdot \epsilon_c$$

where F_{pc} is the view factor from the patch to the cone walls. The view factor can be calculated exactly by means of view factor algebra. The necessary formulas are given in Appendix VI to the Fourth Quarterly Report on Contract NAS5-10113 (15 April 1967). The result is

$$F_{pm} \;=\; 0.7173$$

For the set-up used

$$A_p \;=\; 5.944 \text{ in}^2$$

$$A_i \;=\; 6.822 \text{ in}^2$$

$$K_i \;=\; 3.91 \times 10^{-5} \text{ W} \cdot \text{K}^{-1}$$

A value of σ equal to $3.657 \times 10^{-11} \text{ W} \cdot \text{in}^{-2} \cdot \text{K}^{-4}$ was used in the calculations.

The temperature measurements for two tests on each of the cone wall assemblies are given in Table 4-3.

Table 4-3   Test Cone Measurements

Test No.	Cone Substrate	T_o	T_p	T_c	ϕ_h
1	Hardcoated	91.5	183.6	287.8	0
2	Hardcoated	92.3	197.9	288.5	0.08234
3	Nickelplated	91.4	187.4	293.4	0
4	Nickelplated	91.9	202.5	293.7	0.09821

Temperatures in kelvins; heater power in watts.

The temperatures are averages of from 4 to 7 readings taken over a period of several hours after the system had reached thermal equilibrium. The temperature of the test fixture was raised to at least 55°C and pumped for at least 20 hours prior to cooling the space target with liquid nitrogen. Also, the test fixture was reheated to well above the frost point for the ambient chamber pressure prior to heating the space target back to room temperature. The cone structure (cone and box around the rear of the patch) was connected to a temperature controlled baseplate. The temperature was measured with a copper-constantan thermocouple and a Leeds and Northrup temperature potentiometer (Cat. No. 8692). The patch and space target temperatures were measured with differential chromel-constantan thermocouples to the cone. The heater and differential thermocouple voltages were measured on a Doric Model DS-100 integrating microvoltmeter. The heater current was measured on a Weston Model 902 milliammeter (0-15mA scale).

Next, the tests were repeated without a cone in order to determine the values of ϵ_p and s_i (equation 4-1, with $\epsilon_{pc} = 0$). The patch was heated in all cases to stay close to the temperatures encountered during the cone tests. The results of the measurements and calculations are given in Table 4-4.

Table 4-4 Determination of ϵ_p and s_i

Test No.	T_o	T_p	T_c	ϕ_h	ϵ_p	s_i
5	94.5	208.5	289.0	0.17317		
					0.847	8.085
6	94.35	192.7	289.2	0.06221		
					0.831	8.30
7	94.2	186.1	289.2	0.02422		

The following values were used to calculate ϵ_{pc} from equation 4-1 and the data in Table 4-3.

$$\epsilon_p = 0.84$$

$$s_i = 8.19$$

If we assume both the patch and the space target have the same emissivity ϵ, we obtain

$$\epsilon_p = \epsilon/2-\epsilon$$

For ϵ_p equal to 0.84, ϵ is then 0.91.

The values of ϵ_{pc} and ϵ_c are given in Table 4-5. The value of F_{pc} is 0.2827.

Table 4-5 Cone Wall Emissivities

Test No.	ϵ_{pc}	ϵ_c
1	1.31×10^{-2}	0.0463
2	1.33×10^{-2}	0.0470
3	1.50×10^{-2}	0.053
4	1.25×10^{-2}	0.044

The reproducibility of the tests was considerably greater for the hardcoated sample. The average value of ϵ_c for all four tests is about 0.048.

4.2.2 Effect of Non-Zero Space Target Reflectivity

In addition to decreasing the value of ϵ_p, a non-zero value of space target reflectivity provides alternate paths by which cone wall emission can reach the patch. An estimate of the fraction of cone wall emission that reaches the patch by way of the space target is made below. A black patch is assumed and losses in the cone wall are neglected. In addition, specular reflectivity at the cone walls is assumed.

The fraction of diffuse cone wall emission that reaches the space target directly or by one specular cone wall reflection is

$$F_{cs} + F_{cc} (1 - \epsilon_c) = F_{cs} + F_{cc} = 1 - F_{cp}$$

when cone wall losses are neglected ($\epsilon_c \ll 1$). The factor F_{ij} is the view factor from i to j. The letter c refers to the cone walls, s to the space target (cone mouth), and p to the patch. The fraction reaching the patch after one space target reflection is then $(1 - F_{cp}) \rho_s E_{sp}$, where ρ_s is the diffuse reflectivity of the target and E_{sp} the exchange factor from the target (cone mouth) to the patch. The exchange factor E_{ij} is the fraction of diffusely distributed flux from surface i that reaches surface j directly and by all possible intervening specular reflections (E.M. Sparrow and R.D. Cess, Radiation Heat Transfer, Brooks/Cole, 1966, pp. 140-149). The total fraction of cone wall emission that eventually reaches the patch by reflection in the space target is then

$$r = (1 - F_{cp}) \rho_s E_{sp} [1 + (1 - E_{sp}) \rho_s + (1 - E_{sp})^2 \rho_s^2 + \cdots]$$

$$r = \frac{(1 - F_{cp}) \rho_s E_{sp}}{1 - (1 - E_{sp}) \rho s}$$

By the reciprocity relation, we have

$$A_s E_{sp} = A_p E_{ps}$$

We also have

$$E_{ps} = F_{ps} + (1 - \epsilon_c) F_{pc}$$

$$E_{ps} = F_{ps} + F_{pc} = 1$$

For ϵ_c much less than unity and F_{pp} equal to zero. We then obtain

$$E_{sp} = A_p/A_s$$

The fraction r may be compared with the fraction F_{cp} of cone emission that reaches the patch within the cooler (i.e., without reflection from the space target). The result is

$$\frac{r}{F_{cp}} = \frac{(1 - F_{cp})_{ps} \dfrac{A_p}{A_s}}{F_{cp} \left[1 - \left(1 - \dfrac{A_p}{A_s} \right) \rho s \right]}$$

For the test cone, we have

$$F_{cp} = 0.025$$

$$\frac{A_p}{A_s} = \frac{1}{9}$$

Then, for ρ_s equal to 0.07, we obtain

$$\frac{r}{F_{cp}} = 0.32$$

If ρ_s is reduced to 0.02, this ratio is reduced to 0.088.

The design of the multielement radiant cooler is less sensitive than the test cone to reflections from the space target. First, the cone to patch coupling within the cooler is increased by smaller cone wall angles and multiple reflections. Secondly, the patch to cone wall area ratio is considerably larger.

5.0 COOLER TESTING

During the testing of the radiant cooler, heaters are required on the cone and two patches for:

    a.   Initial outgassing prior to cooler operation (Section 3.0)

    b.   Simulation of earth load on the cone and bias load on the second (90K) patch.

    c.   Variation of cone and patch temperatures to study thermal couplings within the cooler.

Heaters that meet the requirements of (a) and (b) will, in general, also meet those of (c).

The cone, patches, and baseplate (instrument housing) will be raised to 55°C during the initial outgassing. At that time, the space target will be at room temperature. The cone end and patches will therefore be radiating to a blackbody at approximately 20°C. The cone heater power required is very nearly

$$\Phi_1 \;=\; A_d \, \sigma \, (T_c^{\,4} - T_o^{\,4})$$

where A_d =   cone end area = 25.7 in^2

        T_c =   cone temperature = 328 K

        T_o =   space target temperature = 293 K

The result is

$$\Phi_1 \;=\; 3.95 \text{ W}$$

Reducing the baseplate temperature to 25°C has little effect on the heater power needed to maintain the cone at 55°C. Specifically, it increases it by less than 0.1 W.

The earth radiation absorbed in the cone walls is given by (Section 3.0 of the design study report and the monthly report for September 1970).

$$\phi_c \;=\; A_m \, (\alpha_{me} \, W_r + \epsilon_{me} W_e)$$

where A_m =   cone mouth area

        α_{me} =   cone mouth solar absorptivity

        ϵ_{me} =   cone mouth infrared absorptivity

W_r = reflected sunlight exitance of earth = 1.41×10^{-2} W $\cdot$ cm^{-2}

W_e = infrared exitance of earth = 2.1×10^{-2} W $\cdot$ cm^{-2}

For a cone wall solar absorptivity of 0.22 (gold) and infrared absorptivity of 0.05, we have (Section 5.0 of the design study report).

α_{me} = 1.84×10^{-2}

ϵ_{me} = 4.21×10^{-3}

The cone mouth area is 36.55 in^2, so that the above power becomes

ϕ_e = 0.0820 W

For a cone wall infrared absorptivity of 0.07, ϕ_e is increased to 0.0903 W.

A 1 inch x 5 inch area heater will be used on the cone. It has a nominal electrical resistance of 1×10^3 ohms. The nominal voltages (V_c) needed for initial outgassing and for in-orbit simulation are given in Table 5-1.

Table 5-1 Cone Heater Power and Voltage Requirements

ϕ(Watts)	V_c (Volts)
3.95	62.8
0.0820	9.06
0.0903	9.50

Nominal heater resistance = 1×10^3 ohms

The maximum nominal cone heater current is about 63 mA. Such a current is easily carried in vacuum by a 5×10^{-3} inch diameter chromel wire.

The heater power needed on each patch during the initial outgassing is given by

$$\phi_2 = \sigma A_p (T_p^4 - T_o^4)$$

where A_p = black radiating area of patch = 6.40 in^2

T_p = patch temperature = 328 K

T_o = space target temperature = 293 K

This assumes the cone is also at 328 K (55°C). The result is

$$\phi_2 \ = \ 0.984 \ W$$

The bias heat of the detector array on the 90K patch will be replaced by dissipation in the patch heater. This will require a thermal load from about 2×10^{-3} to 4×10^{-3} W. Each patch heater will be a 1×10^3 ohm, 2 W resistor. The voltages required are given in Table 5-2.

Table 5-2   Patch Heater Power and Voltage Requirements

ϕ (Watts)	V_p (Volts)
0.984	31.4
0.002	1.41
0.004	2.00

Nominal heater resistance = 1×10^3 ohms.

.   1.5-volt batteries will be used to provide bias heat. For the 1×10^3 ohm resistance, a 1.5-volt potential results in a dissipation of 2.25×10^{-3} W. Two batteries in series with a 470 ohm dropping resistor will give 4.2×10^{-3} W. Heater leads of 3×10^{-2} inch diameter chromel can be used in all cases.

6.0 MECHANICAL DESIGN

The detailed mechanical design was completed during the first quarter of the construction and test phase of the program. The design of the cooler assembly and cone housing subassembly were updated and detailed, as shown in Figures 6-1 (Dwg. 8114038) and 6-2 (Dwg. 8116242). Nearly all the parts have been fabricated. Still to be completed are the reflective cone and shield walls and the plates for the cooler assembly housing. Fabrication should be complete by the first week of February.

The cone cover actuator has been revised, as shown in Figure 6-3. In the new design, liquid lubrication was eliminated, the electric motor was replaced with a linear solenoid using dry film lubrication, the previous bearings were replaced with no-lube teflon urethane bearings, and the gears modified to alternately mesh aluminum with self-lubricated fiber impregnated polyurethane.

A fixture for the patch vibration test was designed and fabricated, as shown in Figure 6-4. The patch configuration is the same as that in the thermal test model. The vibration test will be completed during January and will be sinusoidal, 5 to 2000 hz, 1 octave per minute, and 20 G's for all three axes.
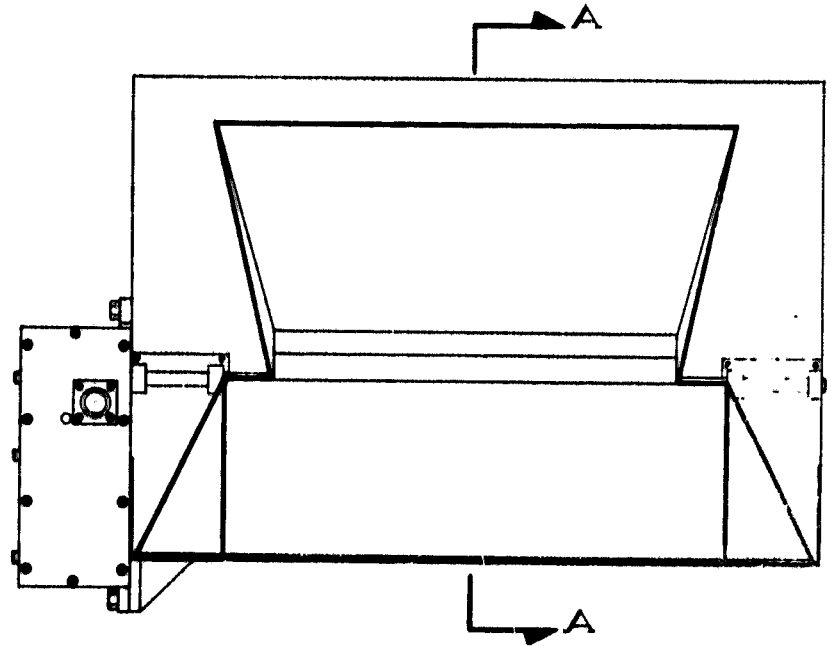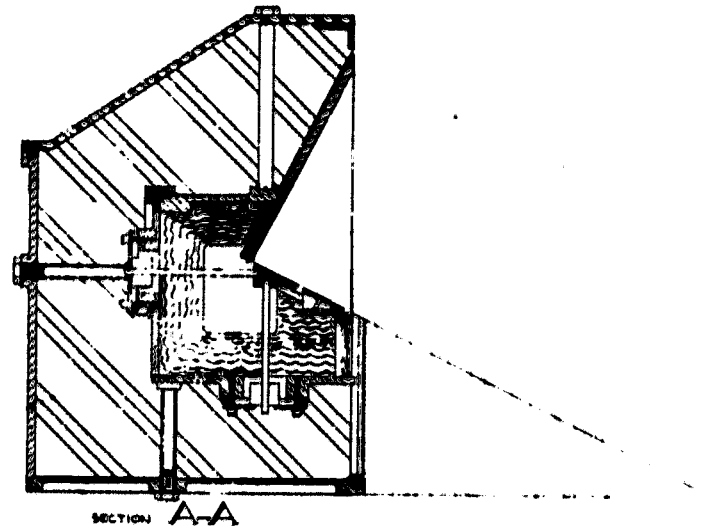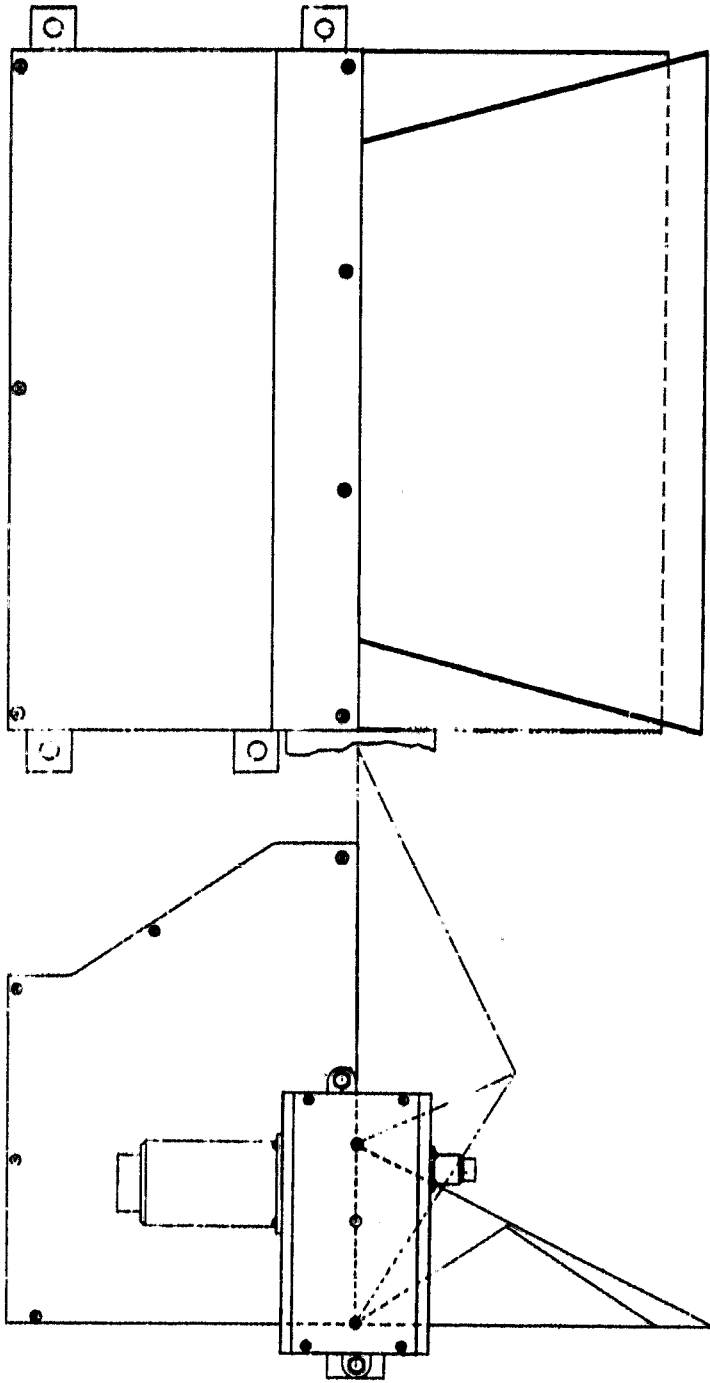
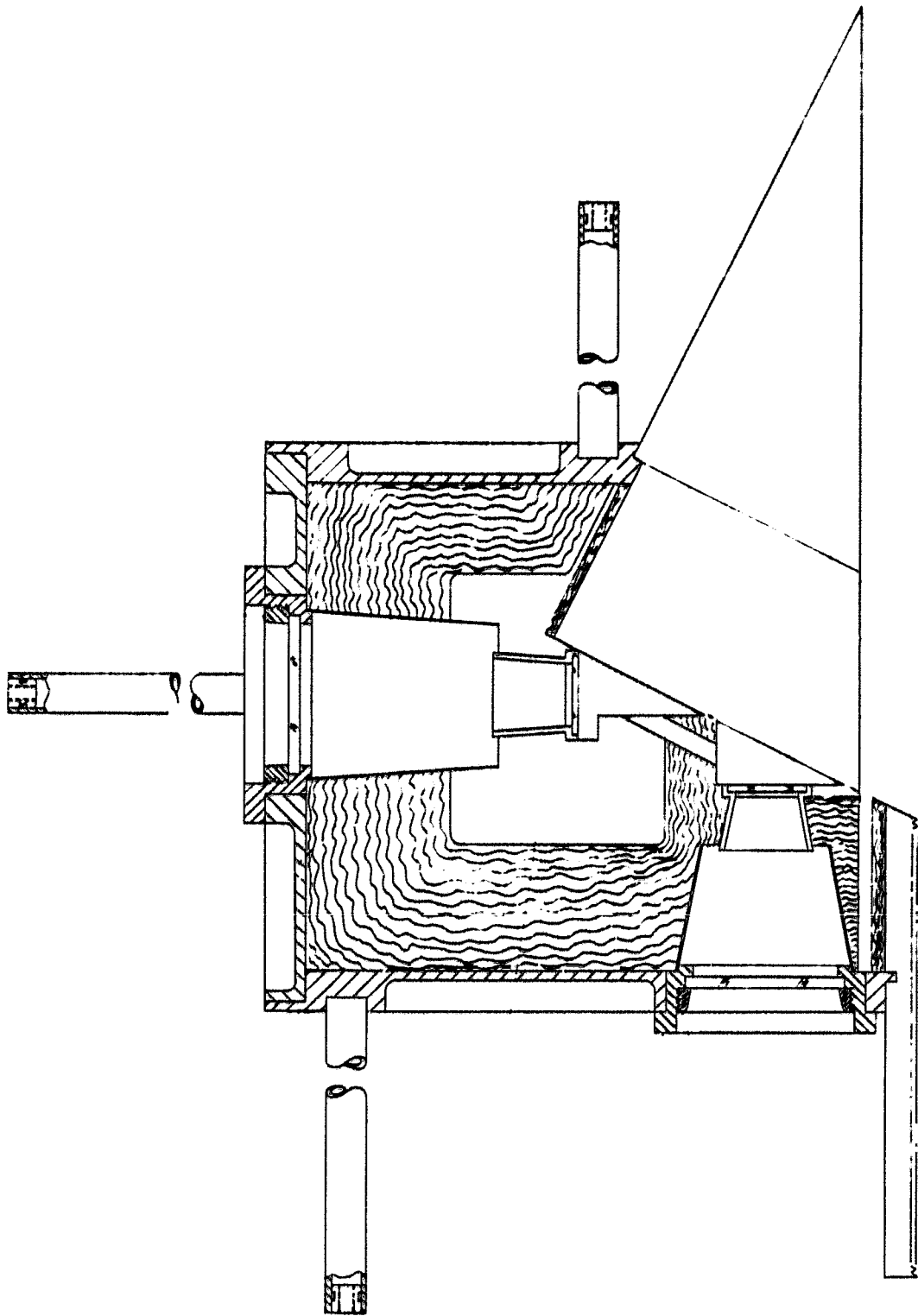SECTION A-A

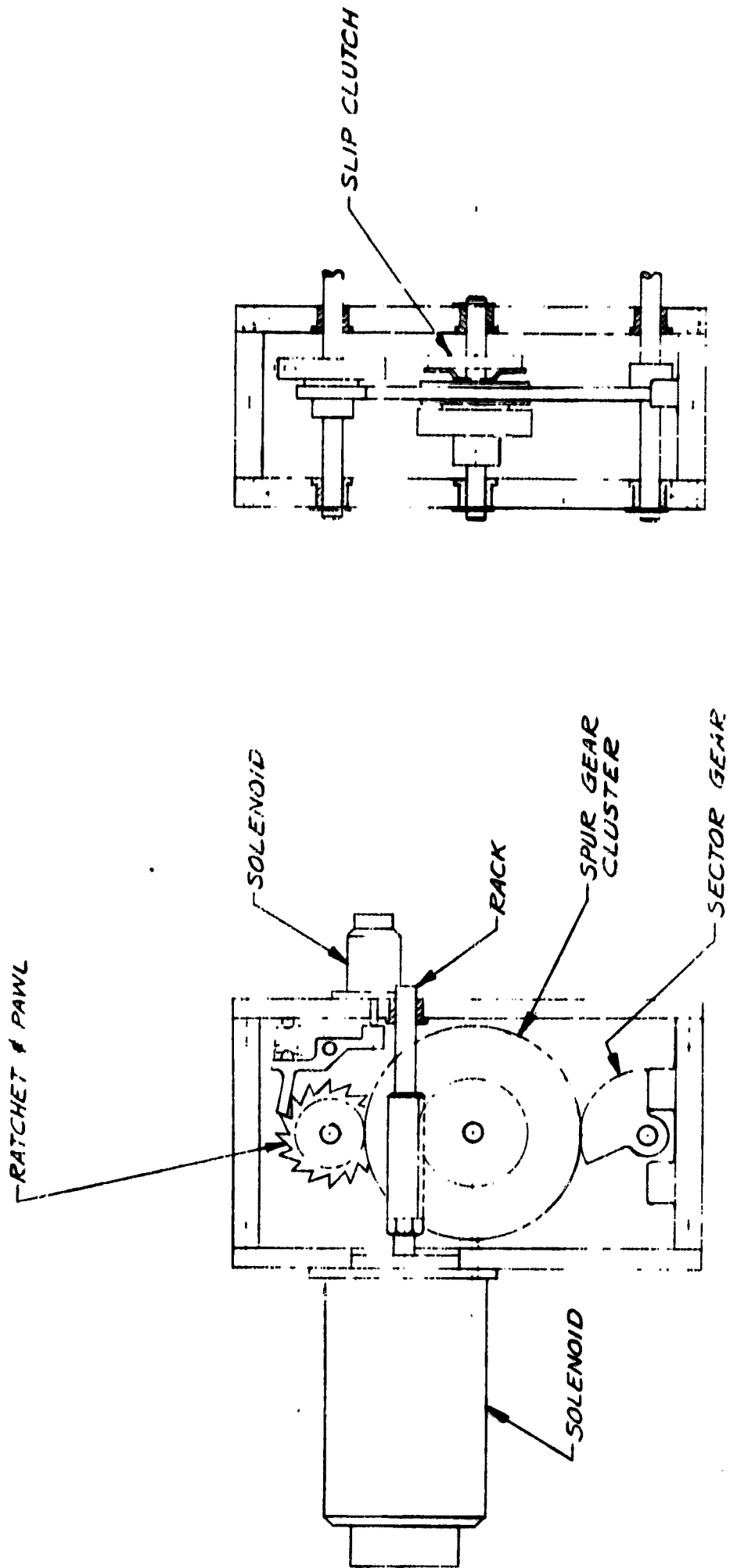Figure 6-1 Radiant Cooler Assembly

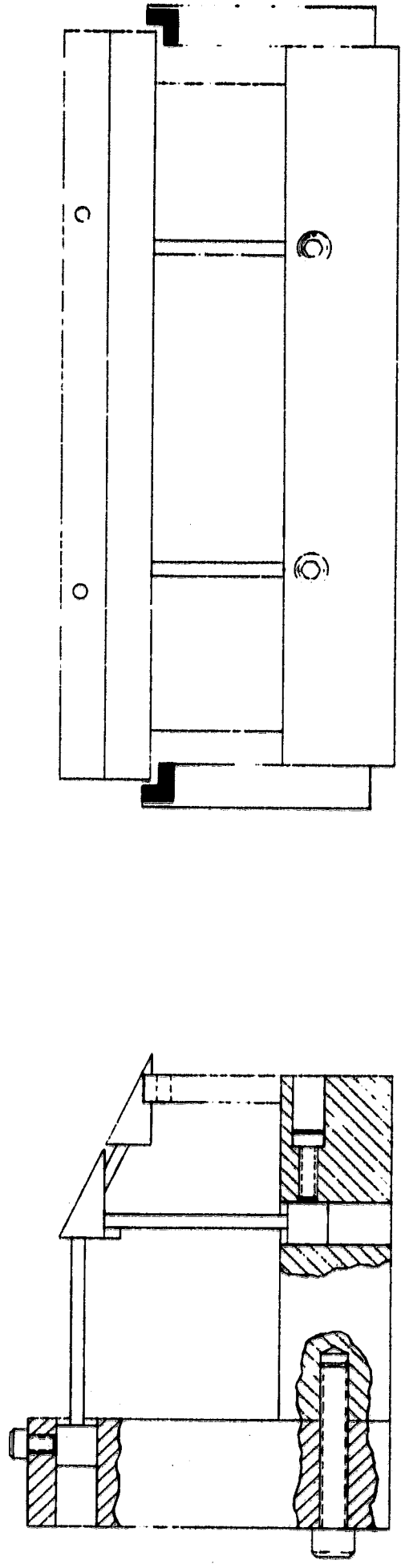Figure 6-2 Cone Housing Assembly

Figure 6-3 Cone Cover Actuator

Figure 6-4 Vibration Fixture and Dual Patch Assembly

7.0 NEW TECHNOLOGY

No items which are considered new technology according to NASA form 1162 were developed during the first quarter of the second contract phase.

8.0 PROGRAM FOR NEXT QUARTER

The present schedule calls for the delivery of the breadboard radiant cooler on April 16, 1971. Hence, construction will have to be completed during the next quarter (17 December 1970 to 17 March 1971) and testing begun. Prior to the start of testing, the cold space target will be installed in the space chamber and the chamber and cooler instrumented for temperature and (heater) power measurements. Sinusoidal vibration tests will be performed on the dual patch assembly. And finally, the studies of insulation and cone surfaces will be continued as time permits.

APPENDIX

SPECIFICATION FOR COOLER

CONE WALL PROCESSING

APPLICATION		REVISIONS			
EXT ASSY	USED ON	LTR	DESCRIPTION	DATE	APPROVED
	61202				

SHEET SIZE																									
REV LETTER																									
SHEET NO.	1	2	3	4	5	6	7	8	9	10	11	12	13	14	15	16	17	18	19	20	21	22	23	24	25

LESS OTHERWISE SPECIFIED DIMENSIONS ARE IN INCHES AND INCLUDE CHEMICALLY APPLIED PLATED FINISHES NOT SCALE PRINT

TOLERANCES

DECIMALS

CONTRACT NO.	
NAS5-21132	
APPROVALS	
DRAWN	
CHECKED	
ENGR	
ITTAOD	
OTHER	

ITT AEROSPACE/OPTICAL DIVISION
FORT WAYNE, INDIANA, U.S.A.
INTERNATIONAL TELEPHONE AND TELEGRAPH CORPORATION

SPECIFICATION FOR COOLER CONE WALL
PROCESSING

SIZE	CODE IDENT NO.		
A	31550	8116057	
SCALE			SHEET 1 of 3

3	ANGLE
PLACE	
2	±.010	±½°

1.0 GENERAL

This specification covers the processing of cone wall sections to be optically finished for cone wall tests. The general process envisioned consists of 5 steps

1. Machining the wall pieces
2. Rough polishing of reflective surface
3. Plating of electroless Nickel (Kanigen® or equivalent)
4. Optical polishing of reflective surface
5. Evaporative coating of reflective layer

The reflective surface is the inner cone wall when the pieces are assembled. This is called out on each drawing.

The goal of this process is to produce an assembled cone that has an extremely low scatter polished surface with high reflectivity. Extreme care will be exercised to protect the surface finish after polishing and reflective coating. Cone assembly will be done by ITT-A/OD.

2.0 APPLICABLE DOCUMENTS

2.1 MIL-I-45208A, "Inspection System Requirements".

2.2 GSFC Spec S-320 - ATS-2, "Environmental Test Specification for Components and Experiments".

2.3 This specification.

3.0 REQUIREMENTS

3.1 Mechanical

3.1.1 Each cone assembly consists of 3 pieces. Each piece is one wall of the cone. The material will be 6061 aluminum processed for stress relieving.

3.1.2 After the wall pieces are machined, the reflective surface will be ground (optical rough polished) to .0002" TIR. The purpose of this step is to provide a flat surface for electroless nickel application to eliminate chance of polishing thru the Ni.

3.1.3 Each piece will be overcoated with a layer of electroless nickel (Kanigen® or equivalent) thick enough to preclude polishing thru to the substrate. Electroless Nickel will be applied over the entire surface of each piece.

DWG	CODE IDENT NO.		
A SIZE	**31550**		8116057
SCALE			SHEET 2 of 3

3.2 Optical

3.2.1 The reflective surface of each piece will then be optically polished to provide an extremely low scatter microfinish. The flatness of the polished side will be to within 5 wavelengths of visible light (10 fringes) over any 2 inch diameter area.

3.2.2 Edge roll off will be limited to within less than 1/16" of the edge.

3.2.3 A highly reflective durable coating of aluminimum will be evaporated onto reflective surface of each piece. No protective overcoat will be applied. The reflectivity of the surface will be .90 or greater at 5500 Å. The reflectivity of one piece in each vacuum run will be measured and supplied to ITT-A/OD. A witness plate processed with each batch may be used for measurements applying to that batch.

3.2.4 There will be no scratches (including hairline scratches), fingerprints, or other defects on the polished surface when viewed with a 10X microscope. There will be no more than 5 pits or digs on each polished surface.

4.0 DOCUMENTATION

The manufacturer shall provide documentation containing the results of all tests and inspections performed on each unit. Data required to comply with Section 3 shall also be provided.

5.0 PREPARATION FOR DELIVERY

Shipping containers shall be entirely suitable to protect each unit shipped during the handling, shipment and storage periods. Packaging and shipment shall conform to "best commercial practices".

VENDOR ACCEPTANCE TEST DATA REPORT

Specification Paragraph No.	Specification Measurement	Part Measurement
3.1.3	Electroless nickel not polished thru	
3.2.1	$\leq$ 10 fringes	
3.2.2	$\leq$ 1/8" on 3 sides; $\leq$ 1/16" on short side	
3.2.4	View with 10X microscope	

6057
3

DWG	CODE IDENT NO.	
A SIZE	**31550**	8116057

SCALE		SHEET 3 of 3